

Banner appropriate to article type will appear here in typeset article

Dynamics of an oscillatory boundary layer over a sediment bed

Jonathan S. Van Doren¹ and M. Housseem Kasbaoui^{1†}

¹School for Engineering of Matter, Transport and Energy, Arizona State University, Tempe, AZ 85281, USA.

(Received xx; revised xx; accepted xx)

We investigate the mechanisms by which a particle bed modifies the oscillatory boundary layer. We perform Euler-Lagrange simulations of an OBL over a particle bed at Reynolds numbers $Re_\delta = 200, 400$, and 800 , density ratio $\rho_p/\rho_f = 2.65$, maximum Shields numbers ranging from 1.42×10^{-2} to 7.40×10^{-2} , Galileo number $Ga = 51.9$, Stokes number ranging from 3.99 to 15.97 , and Kuelegan-Carpenter number ranging from 1.7×10^3 to 6.8×10^3 , and showed large modulation to the underlying boundary layer. We show two mechanisms of modification to the oscillatory boundary layer: (I) the permeability of the bed allows fluid flow to penetrate into the bed, introducing a slip velocity at the bed-fluid interface, an inflection point and the expansion of the boundary layer, and (II) for $Re_\delta = 400$, and 800 , particle motion creates an evolving bedform. For $Re_\delta = 200$, particles are nearly motionless and the permeability of the bed drives the alteration of the velocity profile. The initial bed form drives velocity fluctuations not seen for flow over a smooth, impermeable wall. For Reynolds 400 and 800 particle momentum is associated with the peak velocity fluctuations, indicating that the particle feedback force contributes to velocity fluctuations. We show that the coefficient of friction, computed using the bed shear stress, is decreased by nearly half for Reynolds 200 and 400 , and nearly an eighth for Reynolds 800 .

Key words: keyword 1, keyword 2, keyword 3

MSC Codes (*Optional*) Please enter your MSC Codes here

1. Introduction

In shallow areas of the ocean, the seafloor may be subject to large oscillating pressure gradients and strong shear forces. This causes sediment to become suspended and transported to new locations, where they are deposited as the shear force oscillates. A model flow often used to investigate this process is the oscillatory boundary

[†] Email address for correspondence: houssem.kasbaoui@asu.edu

Abstract must not spill onto p.2

layer (OBL) problem. Stokes (1855) was amongst the first to address this problem, specifically in the limit where viscous effects dominate and where the bottom surface is represented as a smooth flat wall. Under these assumptions, Stokes (1855) derived analytical solutions which show the establishment of a boundary layer with characteristic thickness $\delta = \sqrt{2\nu/\omega}$, where ν is the fluid kinematic viscosity and ω the angular frequency of the oscillations. Due to the assumption of dominating viscous effects, these solutions apply only in the limit of very small Reynolds numbers $Re_\delta = U_0\delta/\nu$, where U_0 is the velocity amplitude of the oscillations. Later, many researchers investigated the dynamics of oscillatory boundary layers over smooth and rough walls at larger Reynolds numbers, including when the Reynolds number is sufficiently high for turbulence to emerge (Akhavan *et al.* 1991*b*; Carstensen *et al.* 2010, 2012; Costamagna *et al.* 2003; Fytanidis *et al.* 2021; Ghodke & Apte 2016, 2018; Hino *et al.* 1976; Mazzuoli & Vittori 2019; Mazzuoli *et al.* 2020, 2016; Ozdemir *et al.* 2014; Pedocchi *et al.* 2011; Salon *et al.* 2007; Sarpkaya 1993; Vittori & Verzicco 1998; Vittori *et al.* 2020). However, it is unclear whether these results are applicable to seafloors. Unlike the previously studied configurations with impermeable and fixed smooth or rough walls, seafloors are made of sediment particles that together form a porous bed. Depending on the details of the flow over it, the bed may be static, with or without bedforms, and may even evolve dynamically as sediment particles saltate or get suspended by the flow (Finn *et al.* 2016). In this manuscript, we investigate the extent to which the OBL is altered by a bottom sediment bed at different Reynolds number.

There has been significant effort devoted to the characterization of the boundary layer that develops over a smooth or rough wall under the action of an oscillatory forcing. Depending on the Reynolds number Re_δ , different regimes have been identified as detailed in (Vittori & Verzicco 1998; Pedocchi *et al.* 2011; Akhavan *et al.* 1991*a*; Ozdemir *et al.* 2014; Fytanidis *et al.* 2021). To summarize, an OBL developing over an impermeable wall exhibits four different regimes. In experiments and simulations with wavy or rough bottom walls, with Reynolds number $Re_\delta \leq 85$ the flow is laminar throughout the oscillation cycle (Blondeaux & Seminara 1979; Vittori & Verzicco 1998; Akhavan *et al.* 1991*a*), and is well described the analytical solutions of Stokes (1855). For larger Reynolds numbers up to ~ 500 with rough or wavy bottom walls, (Hino *et al.* 1976; Jensen *et al.* 1989) or ~ 700 (Blennerhassett & Bassom 2002), the disturbed laminar regime is observed. The latter is characterized by the appearance of small amplitude perturbations superimposed upon the Stokes flow (Vittori & Verzicco 1998). Fytanidis *et al.* (2021) found that the limiting Reynolds number for this regime is dependent on background disturbances, such as initialization parameters. With increasing Reynolds number, the flow enters an intermittent turbulent regime characterized by sudden eruptions of turbulence during the decelerating portion of the oscillatory period before relaminarizing again. The exact value for the transition to intermittent turbulence is dependent upon wall imperfections, background disturbances, and initialization conditions in numerical studies (Vittori & Verzicco 1998). For Reynolds numbers greater than ~ 3460 , Jensen *et al.* (1989) show that the OBL presents sustained velocity fluctuations and a logarithmic-layer for at least 90 percent of the cycle. This criterion defines the turbulent regime.

A number of studies have considered the effects of bottom interfaces upon the structure of the OBL. Jensen *et al.* (1989) experimentally studied smooth beds, rough sandpaper beds, and sand beds. They found that increased roughness relative to the wave height lead to a thicker boundary layer and larger logarithmic layer.

Vittori & Verzicco (1998) investigated the transition to turbulence by simulating an OBL near an imperfect wall. The wall imperfections were modeled through waviness and roughness elements. These imperfections created instabilities that lead to transition. Xiong *et al.* (2020) showed that a temporary roughness element can trigger the formation of a vortex tube which causes the transition to turbulence. Additional studies of roughness effects can be found in (Ghodke & Apte 2016, 2018; Mazzuoli & Vittori 2019). In the case of freely moving particles, Mazzuoli *et al.* (2016) considered a chain of particles resting on a horizontal plane. The particles are shown to form structured chains when set in motion by the OBL. If the particle bed has some waviness then there is also vortex shedding caused by the bed dunes. Finn & Li (2016) proposed a regime map based on the Shields and Galileo number for sediment-turbulence interaction. The Shields number is a nondimensional shear stress, while the Galileo number is the ratio of gravitational forces to viscous forces upon a particle. The Shields number is dependent upon the particle parameters and the flow parameters, while the Galileo number only depends on particle parameters. This leads to a range of potential bedforms with different waviness that may emerge dependent upon the underlying fluid flow. Mazzuoli *et al.* (2020) performed interface-resolved direct numerical simulations of an OBL over a particle bed. They found that particle transport varies between the accelerating and decelerating portion of the flow when the Shields number is small, and is virtually the same when the Shields number is large. The limitation of interface resolved simulations due to high resolution requirements prevents the capture of several bedform periods, which may modulate turbulence. This may further alter particle transport.

To study the OBL, several models can be applied to the study of sediment transport. Namely, Euler-Euler (EE) methods, Euler-Lagrange (EL) methods, and Particle-Resolved Direct Numerical Simulations (PR-DNS). EE methods consider the particle phase as a continuum. Lee *et al.* (2016) developed a 3D EE method using phased based averaging. They showed good predictive capability in sheet flow and scouring simulations. Chiodi *et al.* (2014) derived an EE model for dense viscous flows and turbulent suspensions. They used this method to investigate sediment transport and captured the transition from bedload and suspended load. Maurin *et al.* (2016) compared an EE method with an EL in simulations of turbulent bedload transport and showed agreement between the two methods over a range of Shields numbers. Kasbaoui *et al.* (2019) compared EE simulations with EL simulations for sedimenting particles. They showed that so long as particle clustering is weak, the two methods agree well. Additionally, EE methods are computationally efficient, but are difficult to extract information about particle momentum from. EL formulations provide a high fidelity method for simulating particle-laden flows. EL formulations track individual particles on a separate Lagrangian grid, while the fluid phase is solved on a Eulerian mesh. Capecelatro & Desjardins (2013) used EL formulations previously to simulate dense fluidized beds, and Arolla & Desjardins (2015) used EL methods to reproduce bed-form regimes in slurries in pipe flows. PR-DNS captures detailed information about the particle boundary layer. They have a very high degree of fidelity as they do not rely upon models for the forces on particles. However, this comes at a high computational cost, which restricts their application to smaller domains. Compared to PR-DNS, the EL formulation provides a computationally efficient method for investigating larger fluid domains, which allows meso-scales of the flow to be captured. Importantly, this allows bedforms to emerge as a result of the driving flow, with several periods of the bedform.

In this paper, we study the effect of a cohesionless particle bed on the dynamics

of an OBL from the laminar regime to the onset of turbulence. The structure of the manuscript is as follows. In section 2, we describe the equations that dictate the dynamics of the flow and sediment particles. In section 3, we provide information on the computations and parameters used in this study. In order to understand the role played by the particle bed, we analyze the dynamics of an OBL over a flat plate in section 4, i.e., without particles, as a baseline for comparison. In the following section 5, we analyze the simulations with a particle-bed and highlight the role of suspended particles and bedforms in the modification of the flow regimes. Finally, we give concluding remarks in section 6.

2. Governing equations

We use the volume-filtering approach of Anderson & Jackson (1967) and Euler-Lagrange methodology of Capecelatro & Desjardins (2013) to describe the dynamics of the sediment-laden flow. The carrier phase is an incompressible fluid with density ρ_f and viscosity μ_f . The volume-filtered Navier-Stokes equations read

$$\frac{\partial}{\partial t}(\alpha_f \rho_f) + \nabla \cdot (\alpha_f \rho_f \mathbf{u}_f) = 0, \quad (2.1)$$

$$\frac{\partial}{\partial t}(\alpha_f \rho_f \mathbf{u}_f) + \nabla \cdot (\alpha_f \rho_f \mathbf{u}_f \mathbf{u}_f) = \nabla \cdot \boldsymbol{\tau} + \alpha_f \rho_f \mathbf{g} - \mathbf{F}_p + \nabla \cdot \mathbf{R}_\mu + \mathbf{A}, \quad (2.2)$$

where α_f is the fluid volume fraction, \mathbf{u}_f is the volume-filtered fluid velocity, $\boldsymbol{\tau} = -p\mathbf{I} + \mu[\nabla \mathbf{u}_f + \nabla \mathbf{u}_f^T - \frac{2}{3}(\nabla \cdot \mathbf{u}_f)\mathbf{I}]$ is the resolved fluid stress tensor (Capecelatro & Desjardins 2013), \mathbf{g} is the gravitational acceleration, and \mathbf{F}_p is the momentum exchange between the particles and the fluid. The tensor \mathbf{R}_μ represents the so-called residual viscous stress tensor. This term arises from filtering the point-wise stress tensor. It includes sub-filter scale terms which require closure. This term is believed to be responsible for the apparent enhanced viscosity observed in viscous fluids containing suspended solid particles. For this reason Capecelatro & Desjardins (2013) proposed a closure using an effective viscosity, which when combined with the effective viscosity model of Gibilaro *et al.* (2007) leads to an expression for the residual viscous stress tensor

$$\mathbf{R}_\mu = \mu_f(\alpha_f^{-2.8} - 1)[\nabla \mathbf{u}_f + \nabla \mathbf{u}_f^T - \frac{2}{3}(\nabla \cdot \mathbf{u}_f)\mathbf{I}]. \quad (2.3)$$

In order to study the dynamics of an oscillatory boundary layer, we drive the flow using the last term in equation (2.2), which expresses as

$$\mathbf{A} = \alpha_f \rho_f U_0 \omega \cos(\omega t) \mathbf{e}_x, \quad (2.4)$$

which represents a harmonic pressure gradient forcing with angular frequency ω and amplitude U_0 . Here, x is the coordinate in the streamwise direction along the unitary vector \mathbf{e}_x , y is the coordinate in the wall normal direction, z is the coordinate in the cross-stream direction.

The momentum exchange term \mathbf{F}_p contains contributions due to resolved stresses and drag force. It reads

$$\mathbf{F}_p = \alpha_p \nabla \cdot \boldsymbol{\tau}|_p + f_d \rho_p \alpha_p \frac{\mathbf{u}_f|_p - \mathbf{u}_p}{\tau_p} \quad (2.5)$$

where $\alpha_p = 1 - \alpha_f$ is the particle volume fraction, ρ_p is the particle density, $\tau_p = \rho_p d_p^2 / (18\mu)$ is the response time of a particle with diameter d_p , and f_d represents

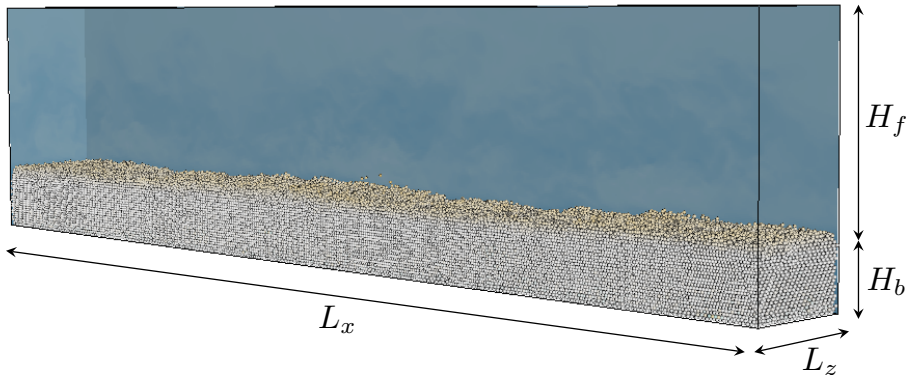


Figure 1: Schematic of the configuration with a bottom sediment bed. The latter is generated in precursor runs where the particles are seeded towards the middle of the domain and allowed to settle on the bottom boundary.

an inertial drag correction. In this study we, use the correction proposed by Tenneti *et al.* (2011) and derived from particle-resolved direct numerical simulations. This correction accounts for inertial and volume fraction effects.

The particles are described in the Lagrangian frame. Following Maxey & Riley (1983), the equations of motion of a particle “ i ” are given by

$$\frac{d\mathbf{x}_p^i}{dt}(t) = \mathbf{u}_p^i(t) \quad (2.6)$$

$$m_p \frac{d\mathbf{u}_p^i}{dt}(t) = V_p \nabla \cdot \boldsymbol{\tau} + m_p f_d \frac{\mathbf{u}_f(\mathbf{x}_p^i, t) - \mathbf{u}_p^i}{\tau_p} + \mathbf{f}_p^{\text{col}} + m_p \mathbf{g} \quad (2.7)$$

where \mathbf{x}^p , \mathbf{u}^p , m_p , and V_p are the particle position, velocity, mass, and volume, respectively. The term $\mathbf{f}_p^{\text{col}}$ represents the collisional force exerted on the particle due to particle-particle and particle-wall collisions. These collision are modeled using the soft sphere model, as detailed in Capecelatro & Desjardins (2013).

Note that the governing equations (2.1) and (2.2) for the fluid phase are solved in both simulations with particles and without. In the latter case, $\alpha_f = 1$ throughout the domain, which recovers the standard Navier-Stokes equations.

We calculate the particle volume fraction and particle velocity from the Lagrangian quantities using

$$\alpha_p(\mathbf{x}, t) = \sum_{i=1}^N V_p g(\|\mathbf{x} - \mathbf{x}_p^i\|) \quad (2.8)$$

$$\alpha_p \mathbf{u}_p(\mathbf{x}, t) = \sum_{i=1}^N \mathbf{u}_p^i(t) V_p g(\|\mathbf{x} - \mathbf{x}_p^i\|) \quad (2.9)$$

where $V_p = \pi d_p^3/6$ is the particle volume. In these equations, g represents a Gaussian filter with width $\delta_f = 7d_p$. Additional details on the computation of these terms, as well as on the solver, can be found in (Capecelatro & Desjardins 2013).

Case	Re_δ	ρ_p/ρ_f	Θ_{\max}	Ga	St_δ	KC
1	200	—	—	—	—	—
2	400	—	—	—	—	—
3	800	—	—	—	—	—
4	200	2.6	1.42×10^{-2}	51.9	3.99	1.7×10^3
5	400	2.6	2.85×10^{-2}	51.9	7.99	3.4×10^3
6	800	2.6	7.40×10^{-2}	51.9	15.97	6.8×10^3

Table 1: Summary of the non-dimensional parameters for the presents runs of an OBL over a smooth wall (runs 1-3) and over a sediment bed (runs 4-6).

3. Numerical experiments

3.1. Configuration

We consider a total of six cases where the Reynolds number is progressively increased from $Re_\delta = 200$ to $Re_\delta = 800$. A summary of the relevant non-dimensional parameters for each run is listed in table 1. In order to provide a baseline for comparisons with the sediment-laden cases, we first investigate the dynamics of an oscillatory boundary layer over a smooth wall, where we vary the forcing amplitude U_0 to yield $Re_\delta = 200, 400$, and 800 . The first two cases are in the laminar regime, so the flow field is expected obey the Stokes solutions (Carstensen *et al.* 2010). The case at $Re_\delta = 800$ is in the intermittent turbulent regime. Each of these cases is then compared to a companion run at the same Reynolds number with a particle bed in order to elucidate the impact of sediment motion, bedforms, and bed permeability on the flow statistics.

The presence of particles introduces additional dimensionless parameters. These are: (i) the density ratio ρ_p/ρ_f , (ii) the Shields number $\Theta_{\max} = \tau_{b,\max}/((\rho_p - \rho_f)gd_p)$, where $\tau_{b,\max}$ is the maximum bed shear stress observed in simulations, (iii) the Galileo number $Ga = d_p\sqrt{(\rho_p/\rho_f - 1)gd_p}/\nu$, (iv) the Stokes number $St_\delta = \tau_p U_0/\delta$, where τ_p is the particle response time, (v) and the Keulegan-Carpenter number, $KC = U_0 T/d_p$. The values for each case is shown in table 1. The work of Finn *et al.* (2016) suggests regimes of particle transport determined by the combination of the Shields and Galileo numbers. Based on their work and the combination of the present parameters, case 4 falls into the “no motion regime”. Cases 5 and 6 fall in the gravitational settling regime. We expect particle motion in both of these cases, with case 6 having higher suspended sediment concentration. Keulegan-Carpenter number is large in all cases, meaning that particle drag will dominate inertial forces associated with the flow oscillations.

Figure 1 shows a schematic of the computational domain used in these simulations. In the single-phase flow simulations, the domain and discretization follow the description in Salon *et al.* (2007). The dimensions are 50δ in the stream-wise direction, 40δ in the wall normal direction, and 25δ in the span-wise direction. For $Re_\delta = 200, 400$ the discretization is 64 points in the stream-wise direction, 256 in the wall normal direction, and 64 in the spanwise direction. For $Re_\delta = 800$ we use a discretization of 256 points in the streamwise direction, 256 in the wall-normal direction, and 128 in the spanwise direction. In order to capture the flow structures near the wall, the mesh is stretched in the wall-normal direction using a hyperbolic tangent function such that the minimum grid spacing is $\Delta y_{\min}/\delta = 0.03$. In simulations with a particle bed, we use a uniform discretization $672 \times 158 \times 67$ such that the mesh spacing Δx is

equal to half a particle diameter. The bedheight is kept at 18.59δ , which gives a depth of 25 particles. This gives a total number of particles $N = 3.1 \times 10^5$. The particle restitution coefficient is held constant at 0.9, as is the particle friction coefficient at 0.1.

The simulation timestep differs from single phase to particle-laden cases. In the single phase cases, we use a period to timestep ratio of $T/\Delta t = 5.6 \times 10^3$. The same ratio in the particle-laden case is $T/\Delta t = 2.24 \times 10^5$. The timestep requirement in the particle-laden case is significantly more restricted. This restriction is driven by the requirement that the bottom layer of the particles must support the weight of the particle bed above them. For more details, see (Capecelatro & Desjardins 2013).

The protocol to initialize the simulations and gathering statistics is as follows. For the single-phase cases at $Re_\delta = 200$ and $Re_\delta = 400$, we initialize the simulations with a quiescent flow and simulate 10 periods of the flow. We discard the first two periods, as they have transient effects from the initialization, and perform phase averaging on the remaining eight periods. For the single-phase case at $Re_\delta = 800$, we find that intermittent turbulence does not emerge within a reasonable simulation time when initializing from a quiescent flow. For this reason, we initialize the flow from an already turbulent flow generated at $Re_\delta = 1790$, that we have previously validated with the experimental data of Jensen *et al.* (1989). This provides sufficient initial disturbances for the flow to trigger intermittent turbulence at $Re_\delta = 800$. We run the simulation for several periods until the flow reaches a stationary state, which requires 2 periods for cases 1-2 and 4-6. Case 3 requires 4 periods to reach stationary state because it is initialized from a highly turbulent flow field. This is validated by confirming that fluid velocity statistics no longer vary with additional periods. After this, we collect data over the following 8 periods for the purpose of phase-averaging. For cases with a sediment-bed, we perform precursor simulations to generate a realistic poured-bed as described in §3.2. Then, we carry out simulations initialized from quiescent flow. Monitoring changes to the flow statistics from period to period shows that transient effects due to the initialization are gone with 4 periods. We then, simulate for additional 8 periods to collect statistics.

3.2. Bed formation and bed-fluid interface

To form the sediment bed in cases 4-6, we perform precursor simulations that serve to generate a realistic bed volume fraction that matches the volume fraction of a poured bed, about 63% (Scott & Kilgour 1969). In these runs, the oscillatory forcing is turned off and the particles are initially uniformly distributed towards the middle of the domain at an average volume fraction of 40% and with small random velocity fluctuations. We then integrate the governing equations (2.1), (2.2), (2.6), and (2.7) until the particles fully settle down. Particle-particle collisions and fluid-mediated particle-particle interactions lead to the formation of the poured bed in figure 1.

Figure 2a shows the average particle volume fraction $\langle \alpha_p \rangle_{xz}$ profile as a function of the wall normal distance. Note that here and onward, the notation $\langle \cdot \rangle_{xz}$ refers to ensemble and spatial averaging over the streamwise (x) and spanwise (z) directions. As anticipated, the volume fraction within the bed matches the random poured packing (Scott & Kilgour 1969). It smoothly transitions to zero away from the bed. Further, we conduct the simulations with particle beds that are sufficiently deep to ensure that the interaction between the particle bed and the turbulent flow above is captured without interference from the bottom boundary. In the present study, the sediment bed is thick by about 25 particle diameters, which corresponds to about $\sim 8.30\delta$.

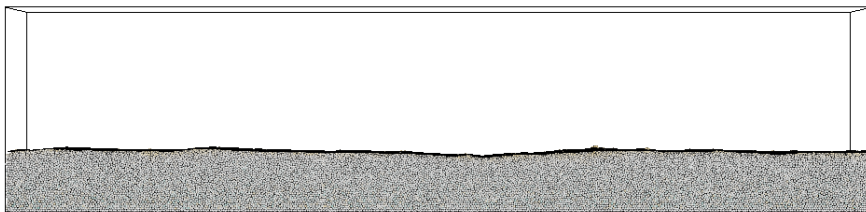
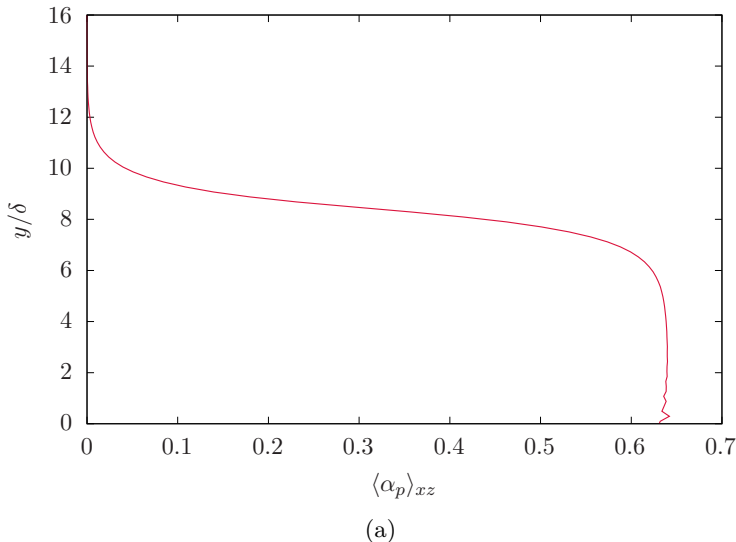


Figure 2: The particle bed is initialized by letting particles settle onto the bottom wall. (a) This procedure results in a volume fraction profile that is consistent with that of a poured bed. (b) The isosurface $\alpha_p = 0.2$ represents a good indicator of the location of the bed-fluid interface.

At this point, we must address the way we define the bed-fluid interface. We follow the approach of Kidanemariam & Uhlmann (2014), where we define the bed-fluid interface using an isosurface of the particle volume fraction $\alpha_p = \alpha_{p,b} < 0.63$. However, it is important to recognize that the choice of the isosurface $\alpha_{p,b}$ demarcating the bed-fluid interface is somewhat arbitrary since the computation of the volume fraction field α_p depends on numerical choices. For example, the shape and size of the filter kernel used to compute α_p control the width of the transition region in figure 2a. With the filtering described in §2, the isosurface $\alpha_{p,b} = 0.2$ provides a good indicator of the approximate location of the bed-fluid interface. We determine this by verifying that this surface lies right on top of the particles as shown in figure 2b.

4. Structure of an Oscillatory Boundary Layer over a smooth wall

We now turn our attention to cases 1-3, where the bottom boundary is an impermeable smooth wall rather than a sediment bed. The reasons for this are twofold. First, analytical solutions exist for the laminar regime, which allows the validation

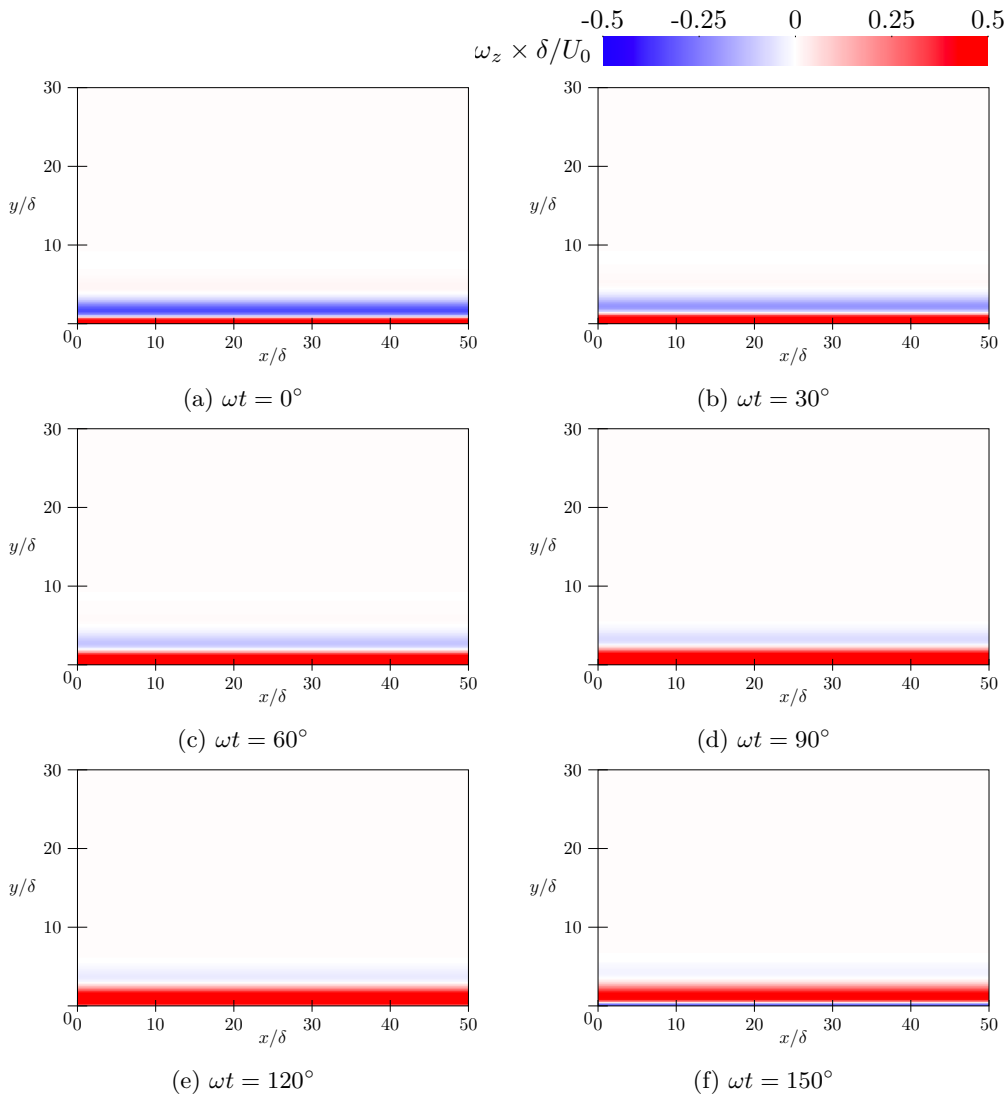


Figure 3: Normalized spanwise vorticity fields at $Re_\delta = 400$ for a smooth, impermeable wall, at phases 0, 30, 60, 90, 120 and 150 degrees. The vorticity is arranged in laminae at all phases.

of the computational approach. Second, these runs serve as benchmark to elucidate the changes to the flow in presence of a sediment bed.

Figure 3 shows the normalized spanwise vorticity field at phases $\omega t = 0, 60, 90, 120$, and 180° for the case at Reynolds 400. The solution at Reynolds 200 shows similar vorticity structure to the Reynolds 400 and, thus, is not included here. The vorticity in these low Reynolds number cases, is organized into sheets in the near-wall region. This indicates laminar flow, and so the flow at Reynolds 200 and 400 should obey the Stokes solution,

$$u_{f,x}/U_0 = \cos(\omega t) - e^{-y/\delta} \cos(\omega t - y/\delta), \quad (4.1)$$

$$u_{f,y}/U_0 = 0. \quad (4.2)$$

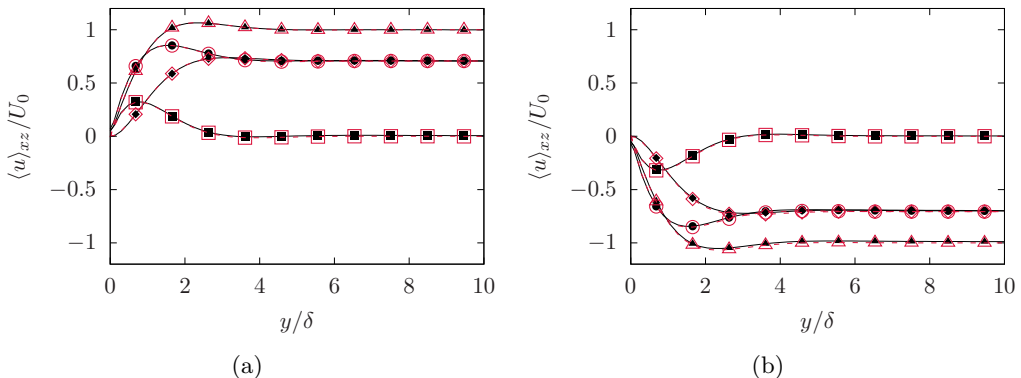


Figure 4: Normalized stream-wise velocity for the case of an OBL over an impermeable smooth wall at $Re_\delta = 400$ during (a) the positive velocity half cycle, and (b) the negative velocity half cycle. Solid black lines with symbols correspond to the Stokes solution, while dashed red lines with symbols correspond to simulation data. The symbols indicate the phase: ($\square, \omega t = 0, 180$), ($\circ, \omega t = 45, 225$), ($\triangle, \omega t = 90, 270$), ($\diamond, \omega t = 135, 315$). The strong agreement between the simulated data and the Stokes solution indicates that the flow is fully laminar in this case.

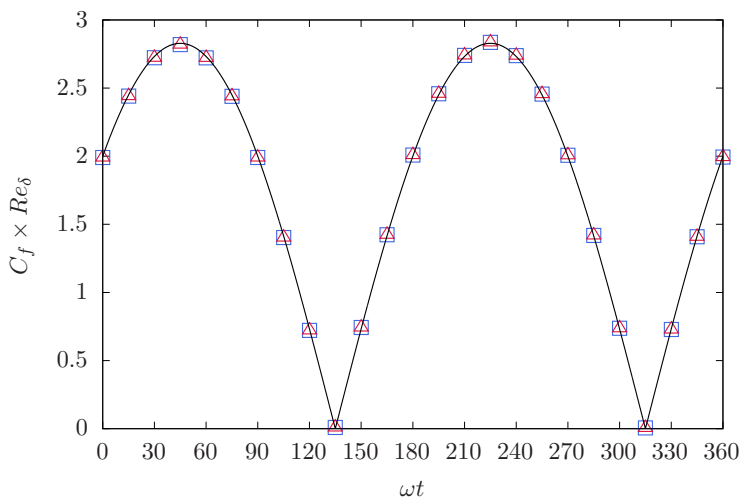


Figure 5: Scaled coefficient of friction over one period at $Re_\delta = 200$ and 400 , for a smooth, impermeable wall. The black line correspond to the Stokes solution. Symbols correspond to the numerical solution at ($\square, Re_\delta = 200$) and ($\triangle, Re_\delta = 400$). All cases collapse onto the Stokes solution.

To verify this, we compare the Stokes solution to vertical profiles of the phase-averaged fluid velocity from the simulation at $Re_\delta = 400$ in figure 4. The agreement between the simulated data and the analytical solution is excellent, showing that the flow is indeed laminar at these Reynolds numbers. This also validates the computational approach for an impermeable smooth wall oscillatory boundary layer at low Reynolds numbers.

As an additional comparison, we compute the coefficient of friction C_f defined as,

$$C_f = \frac{|\tau_w|}{(1/2)\rho_f U_0^2}, \quad (4.3)$$

where τ_w is the wall shear stress. Figure 5 shows the variation of the coefficient of friction scaled by Re_δ . This cancels the Reynolds number dependence of the coefficient of friction. The scaled coefficient is plotted over a period for the cases of an OBL over an impermeable smooth wall at $Re_\delta = 200$ and 400, alongside the Stokes solution. Here too, the agreement between numerical and Stokes solution is excellent which further demonstrates that the OBL at these Reynolds number is fully laminar.

Unlike the lower Reynolds number cases, figure 6 shows significant vorticity throughout the cycle for the case at $Re_\delta = 800$. Of particular interest is the range of scales seen at phase 120° , which is in the decelerating portion of the cycle. This eruption of velocity fluctuations, followed by partial relaminarization, is characteristic of the intermittent turbulence regime. Similar observations were made by Jensen *et al.* (1989), Vittori & Verzicco (1998), and Salon *et al.* (2007).

The vorticity field for Reynolds 800 indicates the possibility of turbulence. To investigate this further, we plot the spatially averaged streamwise velocity in semilog, shown in figure 7. The velocity is normalized using wall units, i.e., the friction velocity $u_\tau = \sqrt{\tau_w/\rho_f}$ as velocity scale and ν/u_τ as length scale. The profiles do not show a logarithmic layer. The smooth wall baseline flow does not exhibit turbulence.

5. OBL over a cohesionless particle bed

Having characterized the dynamics in the case of a bottom smooth flat wall, we now analyze the changes that occur when the oscillatory boundary layer develops over a cohesionless particle bed.

5.1. Case at $Re_\delta = 200$

While in the case of an OBL over a smooth impermeable wall at $Re_\delta = 200$ the flow is devoid of any fluctuations, the presence of a sediment bed leads to notable vortex shedding. These dynamics are visible in figure 8 depicting the spanwise vorticity in a wall normal plane at different phases of the cycle. To highlight the bedform, figure 8 also shows the volume fraction contour $\alpha_p = \alpha_{p,b} = 0.2$ that demarcates the sediment bed-fluid interface. The latter displays small waviness which results in some vortex shedding. These structures are small departures from the single phase case, showing a shift in the presence of a bedform, towards the disturbed laminar regime.

The mean velocity profile is altered by the cohesionless particle bed. Figure 9 shows the average velocity profiles for Reynolds 200. To compare the two-phase velocity profile to the analytical solutions, the vertical distance is shifted by the average bed height at initialization, that is, the average y location for volume fraction 0.2. In these cases, the bed does not evolve significantly and so the average bed height does not meaningfully change throughout the simulation. Reynolds 200 is close to the analytical solution, but with some important deviations. Specifically, the boundary layer is thicker, and there is an inflection point near the bed interface. Additionally, the velocity does not become zero immediately within the bed, showing flow intrusion within the bed. The flow intrusion leads to a thicker boundary layer in the presence of a bed. Finally, the maximum velocities within the boundary layer is decreased.

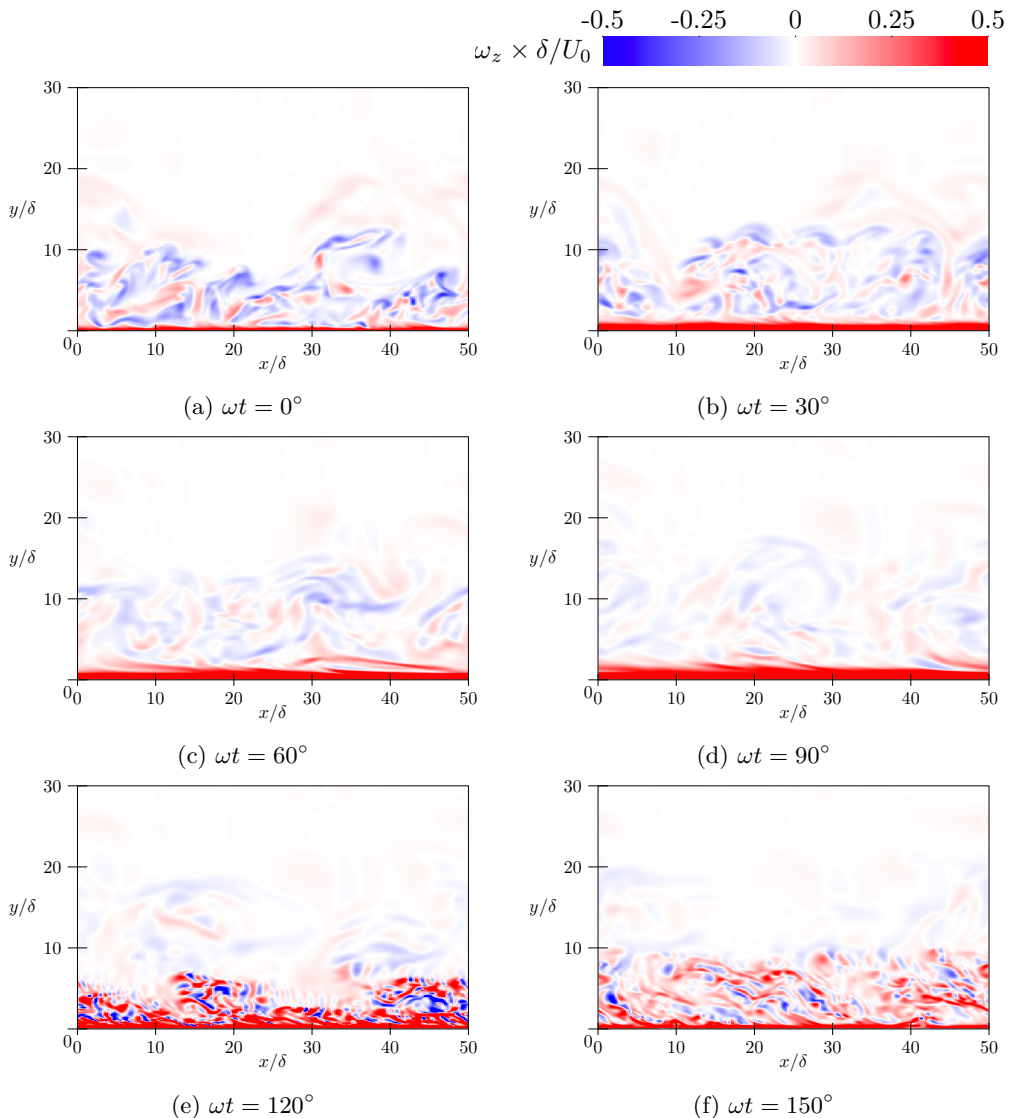


Figure 6: Normalized spanwise vorticity field in DNS of an OBL over an impermeable smooth wall at $Re_\delta = 800$, for a smooth, impermeable wall. The eruption of velocity fluctuations during the decelerating portion of the cycle (120° and 150°) indicates that this flow is in the intermittent turbulent regime.

The presence of a particle bed leads to greater velocity fluctuations than in the smooth wall cases. Figure 10 shows the streamwise velocity fluctuations. The rms fluctuations for a smooth wall at Reynolds 200 is zero throughout the water column. However, the presence of a particle bed leads to non-zero fluctuations. For Reynolds 200, there are peaks near 10 percent of the forcing amplitude at $1d_p$ above the bed. The fluctuations show multiple peaks for all phases except 150. This indicates repeated structures at fixed heights above the bed.

The particle bed leads to a different condition at the fluid-bed interface as compared to a smooth wall. In the smooth wall case, no-slip applies at the wall, while the

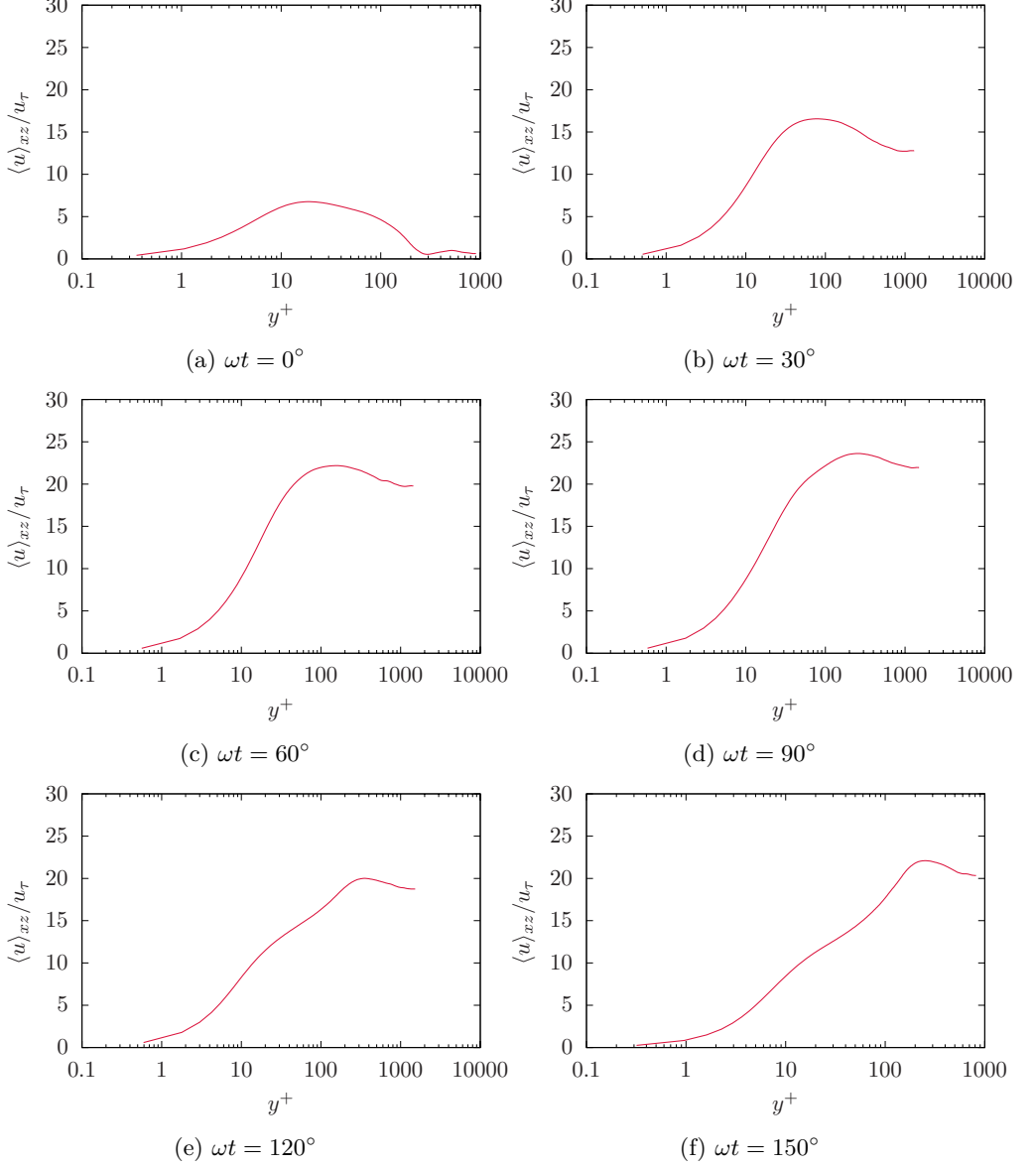


Figure 7: Wall scaled mean velocity profiles for $Re_\delta = 800$, for a smooth, impermeable wall. No logarithmic layer is observed.

particle bed is porous, which leads to a slip velocity at the fluid-bed interface. This causes the bed shear stress to be reduced compared to the smooth wall case. We define the bed shear stress as the shear stress conditioned on an isosurface corresponding to the bed interface $\alpha_p = \alpha_{p,b}$.

$$\tau_b = ||\langle \mathbf{n} \cdot \boldsymbol{\tau}' |_{\alpha_p = \alpha_{p,b}} \rangle|| \quad (5.1)$$

where \mathbf{n} is the normal vector on the isosurface $\alpha_p = \alpha_{p,b}$, and $\boldsymbol{\tau}' = \mu[\nabla \mathbf{u} + \nabla \mathbf{u}^T - (2/3)(\nabla \cdot \mathbf{u})\mathbf{I}] + \mathbf{R}_\mu$ is the deviatoric stress tensor. With the closure of Gibilaro *et al.*

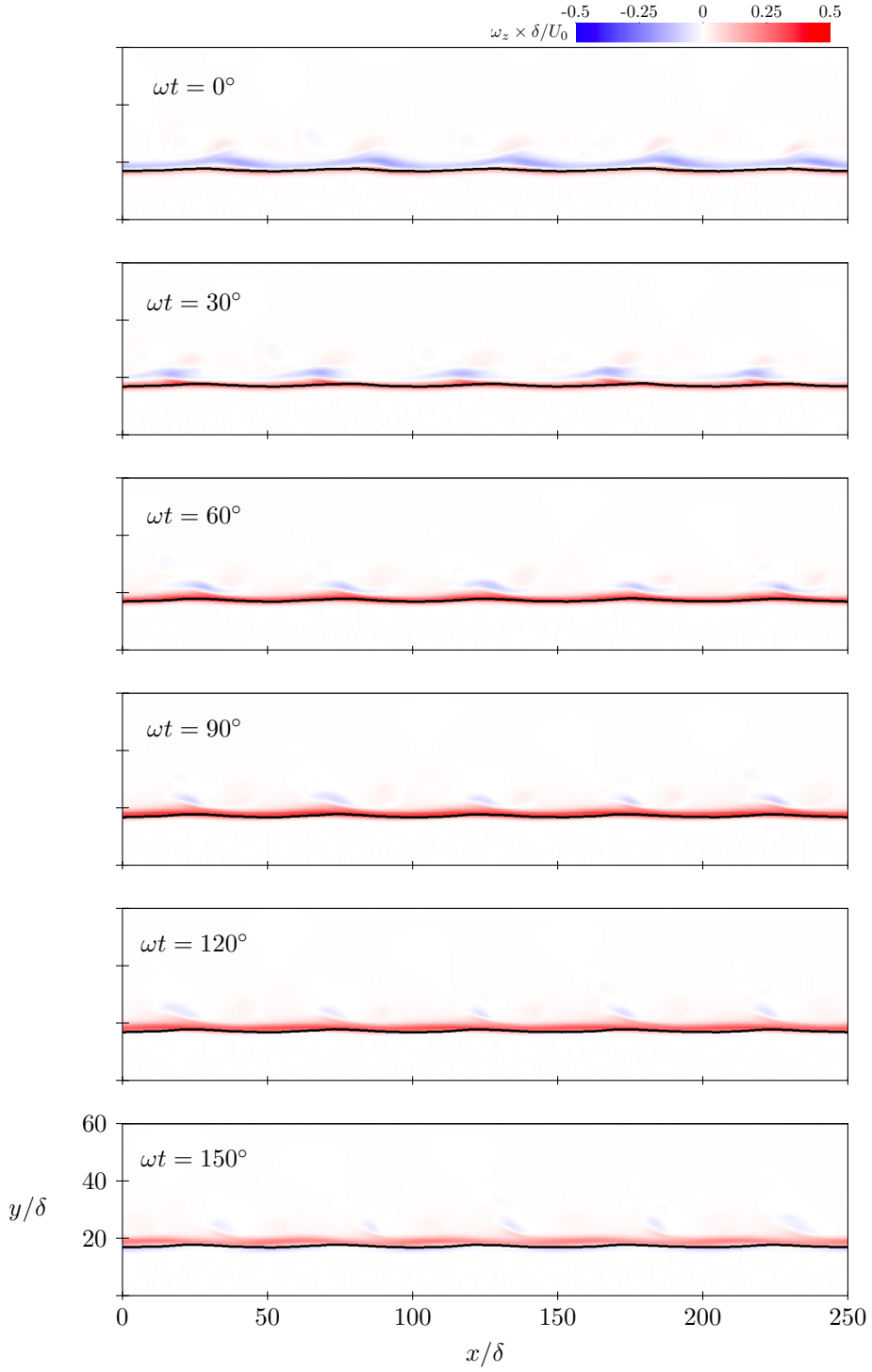


Figure 8: Span-wise vorticity fields at $Re_\delta = 200$, at phases 0, 30, 60, 90, 120, and 150 degrees. Small ripples in the bedform cause repeated shedding vortices to emerge.

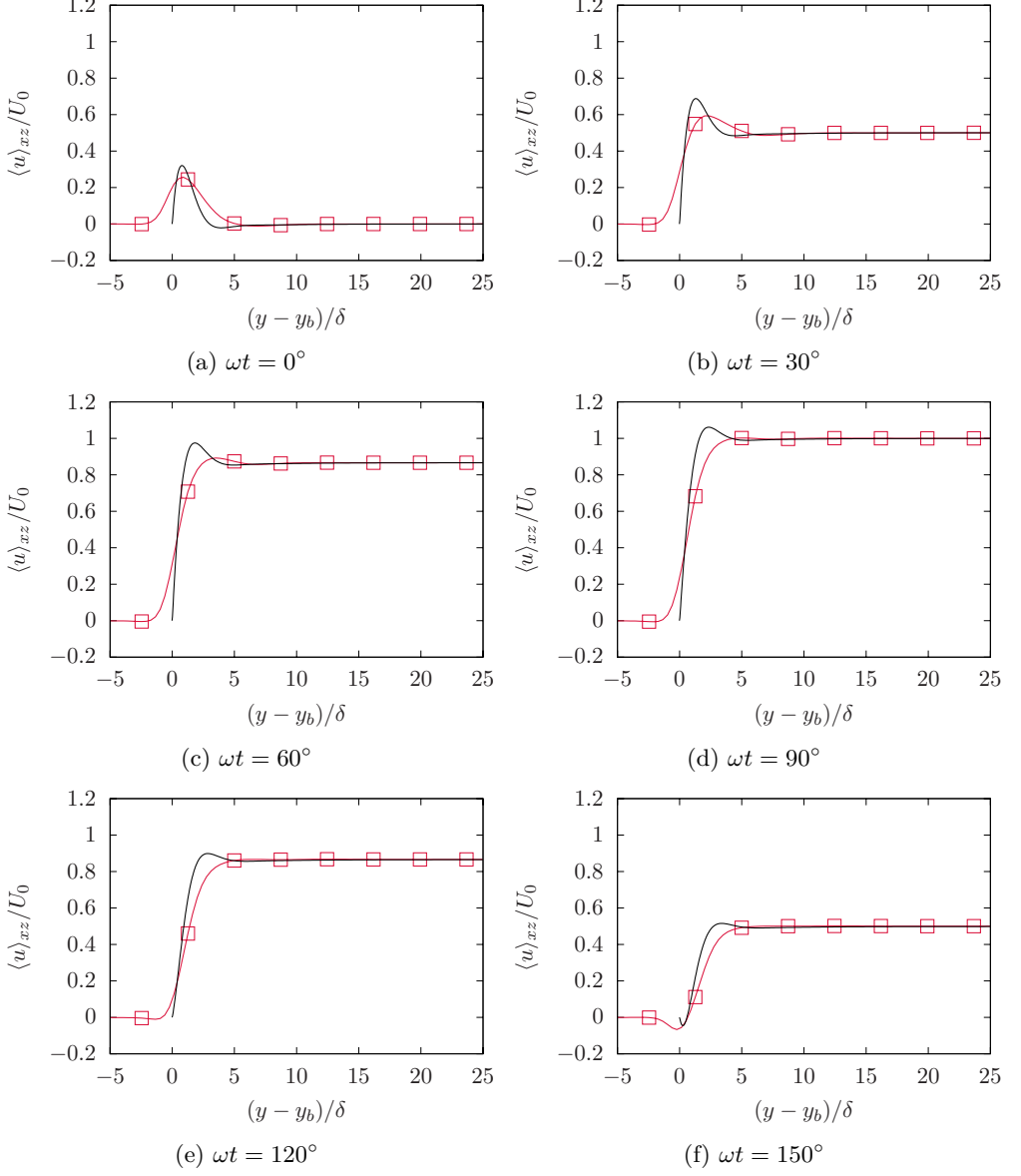


Figure 9: Profiles of the mean streamwise velocity at $Re_\delta = 200$. The profiles are given at phases 0, 30, 60, 90, 120, and 150. Red lines with symbols correspond to simulations with a particle bed, black lines correspond to smooth wall simulations.

(2007), this tensor reads

$$\boldsymbol{\tau}' = \mu \alpha_f^{-2.8} \left(\nabla \mathbf{u} + \nabla \mathbf{u}^T - (2/3)(\nabla \cdot \mathbf{u}) \mathbf{I} \right) \quad (5.2)$$

The deviatoric stress is computed throughout the domain, and then interpolated to the bed surface. We spatially average the stress over the bed, and then take the

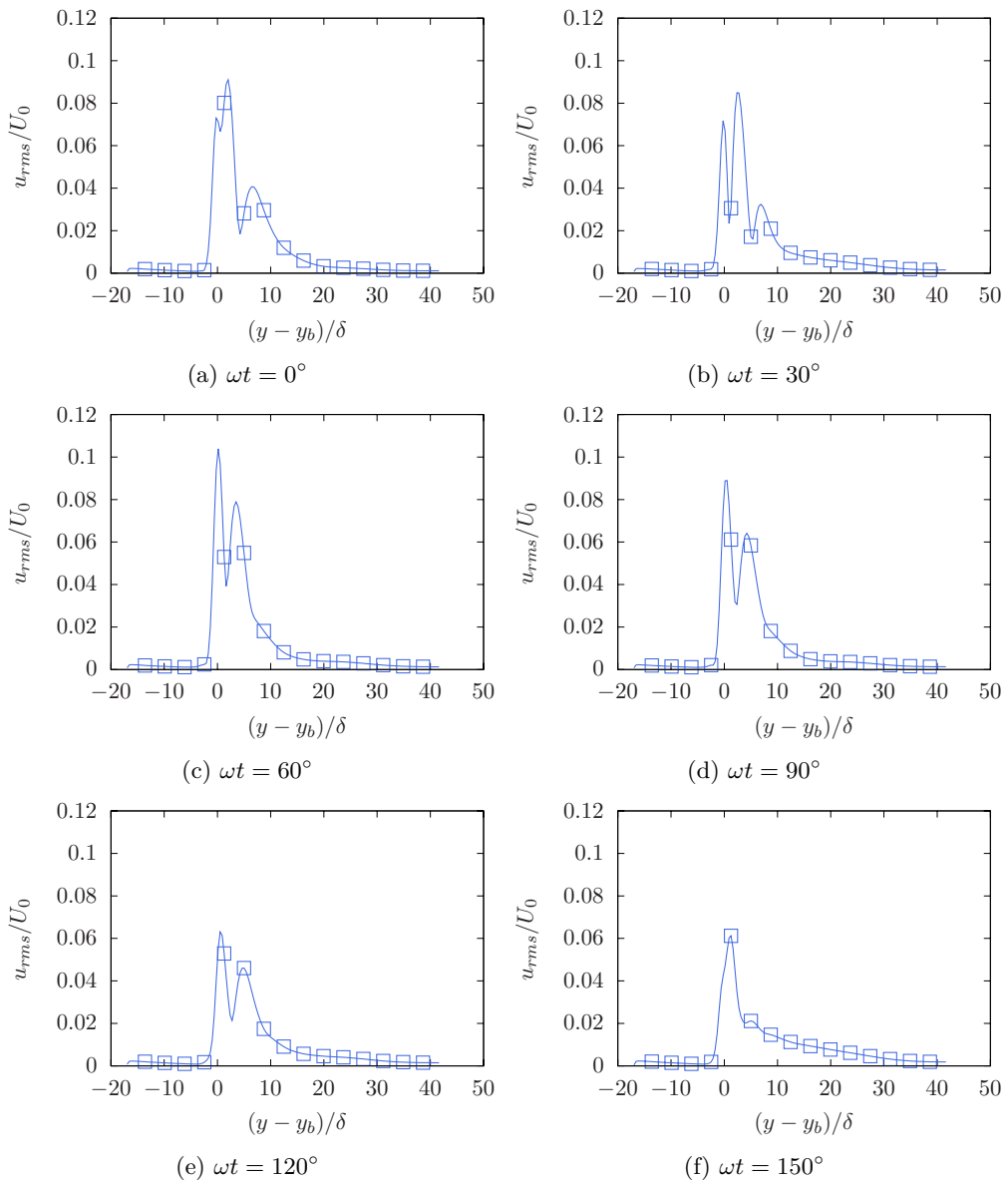


Figure 10: Profiles of the rms fluctuations of the streamwise velocity at $Re_\delta = 200$, in presence of a particle bed. The profiles are given at phases 0, 30, 60, 90, 120, and 150. Even at Reynolds 200 velocity fluctuations are non-zero in the presence of a particle bed, whereas fluctuations are zero throughout the water columns for a smooth wall.

magnitude. We define the coefficient of friction at the bed interface as

$$C_f = \frac{\tau_b}{(1/2)\alpha_f \rho_f U_0^2} \quad (5.3)$$

The coefficient of friction scaled by Re_δ is plotted in figure 11 as a function of time for Reynolds 200. The amplitude of the coefficient of friction is reduced by 40 percent. The phase is shifted by 30° . The analytical phase shift for the coefficient of friction

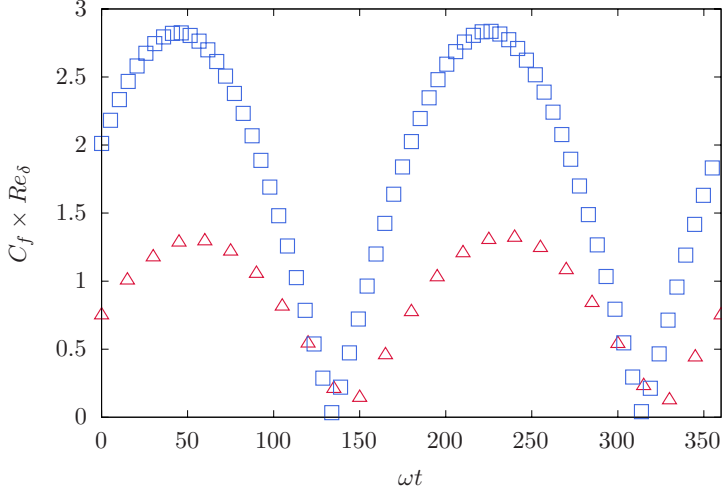


Figure 11: Coefficient of friction for an OBL over a particle bed at $Re_\delta = 200$. Red symbols corresponds to the particle bed case, blue symbols correspond to the smooth wall case. The coefficient of friction is reduced in amplitude by nearly half in the presence of a particle bed. The phase is shifted by 30° .

in the laminar regime is 45° , showing a departure even at low Reynolds number from the analytical behavior. The reduction in coefficient of friction is caused by the change in boundary condition near the wall, which leads to an inflection point in the streamwise velocity.

5.2. Case at $Re_\delta = 400$

The disturbances caused by the small bedform increase significantly at $Re_\delta = 400$. Figure 12 shows the instantaneous spanwise vorticity at $Re_\delta = 400$. We note significantly greater vortex shedding, particularly at phases 90° and 120° . The vortex structures observed at those phases show a chaotic behavior. The larger structures spin off and break down into smaller scale structures. However, the range of scales is limited compared to what may be expected for a fully turbulent flow. Still, the presence of vortex shedding shows a process through which turbulence can emerge at much lower Reynolds numbers than over an impermeable smooth wall, as large vortices shed by small ripples in the particle bed break into smaller flow structures. The vorticity does not penetrate more than one Stokes thickness. Flow intrusion leads to particle transport by creating a seepage flow. Where the flow intrusion leaves the bedform, the flow exerts drag on particles, which causes particle transport, as described in Jewel *et al.* (2019). The outflow from the bed may set some particles into motion. The bedform, demarked by a black line in figure 12, changes with the phase. This shows that particles are transported by the flow. Figure 13 shows the average velocity profiles for Reynolds 400. While the smooth wall case showed good agreement with the laminar solution for $Re_\delta = 400$, the OBL over a particle bed the profile is significantly altered. The velocity profile shows flow penetration within the bed, to a depth of up to 2.5δ . This leads to an inflection point within the boundary layer, and a reduction in the gradient of the streamwise velocity. For all phases, the boundary layer is significantly thicker in the presence of the bed. The maximum

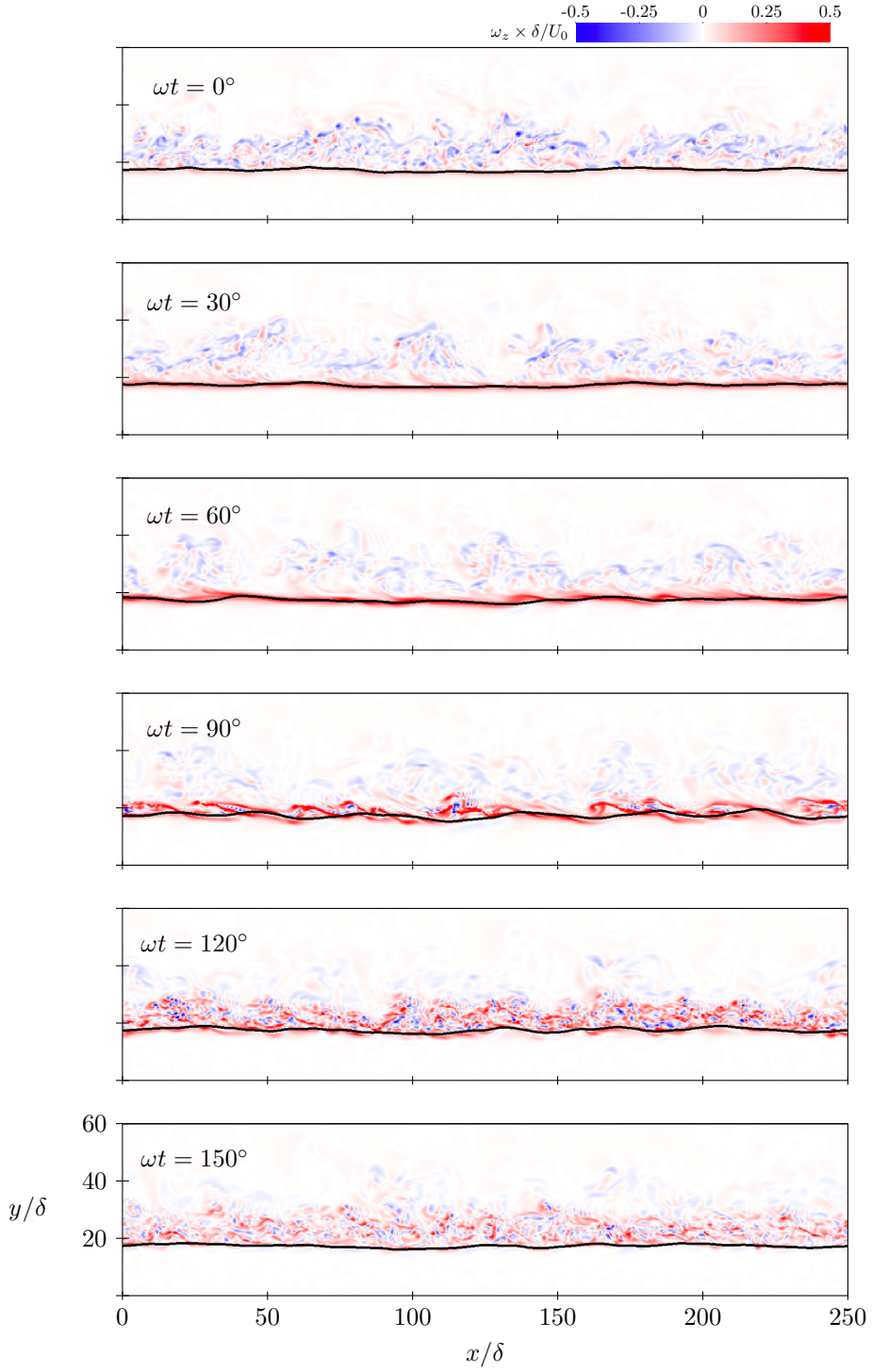


Figure 12: Span-wise vorticity fields at $Re_\delta = 400$, at phases 0, 30, 60, 90, 120, and 150 degrees. Increasing Reynolds number leads to greater vortex shedding, with small non-repeating vortices emerging at Reynolds 400.

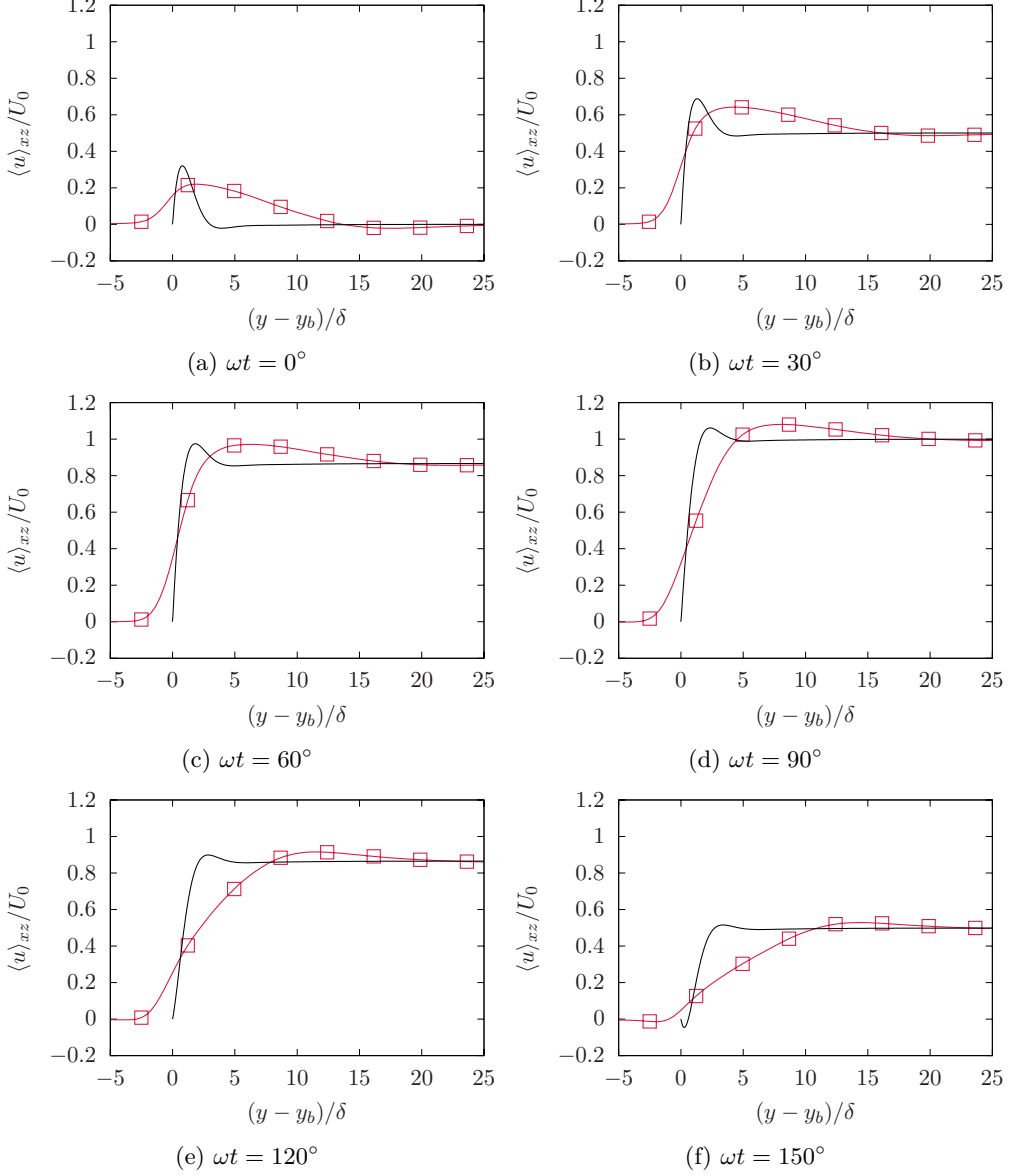


Figure 13: Profiles of the mean streamwise velocity at $Re_\delta = 400$, in the presence of a particle bed. The profiles are given at phases 0, 30, 60, 90, 120, and 150. Red lines with symbols correspond to simulations with a particle bed, black lines correspond to smooth wall simulations.

velocity in the boundary layer is decreased in the presence of a particle bed for phases 0 and 30 degrees.

The presence of a particle bed leads to greater velocity fluctuations than in the smooth wall cases. Figure 14 shows the streamwise velocity fluctuations. The rms fluctuations for a smooth wall at Reynolds 400 are zero throughout the water column. However, the presence of a particle bed leads to non-zero fluctuations. Reynolds 400 shows a peak at 20 percent of the forcing amplitude at phase 90 degrees, located

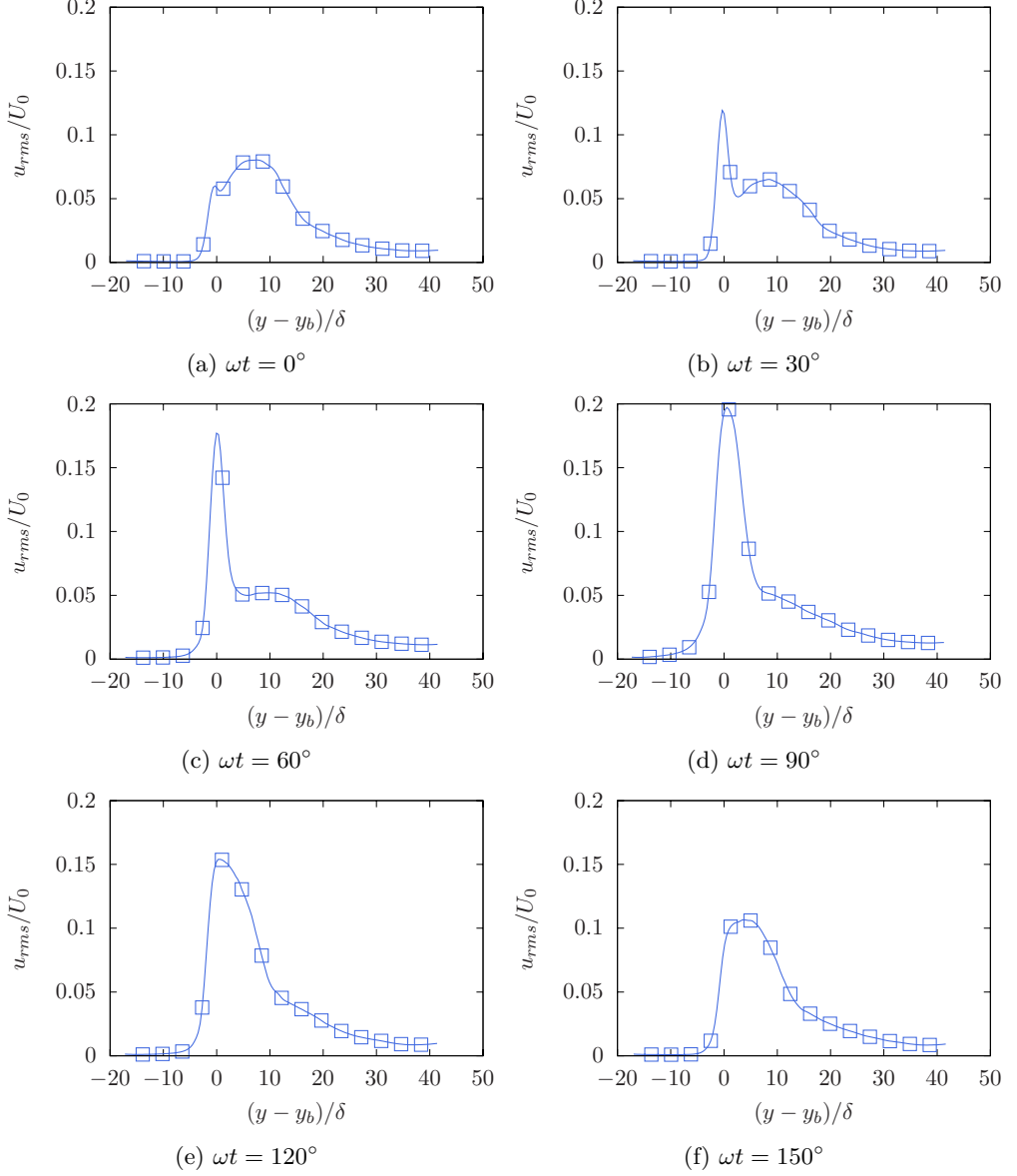


Figure 14: Profiles of the rms fluctuations of the streamwise velocity at $Re_\delta = 400$, in presence of a particle bed. The profiles are given at phases 0, 30, 60, 90, 120, and 150. Velocity fluctuations show a thick single peak near the bed, indicating randomness in the fluctuations.

at $0.25d_p$ above the bed. This indicates that the larger fluctuations are generated at the fluid-bed interface, possibly by saltating particles. Additionally, we observe single peaks near the bed interface for all phases except $\omega t = 30^\circ$. The thickened single peak indicates randomness in the fluctuations.

To investigate the particle motion we show the particle momentum in figure 15. The particle momentum is negligible $5.9d_p$ below the bed interface. For all phases, the particle momentum begins to increase near $1.5d_p$ below the bed interface. Phase

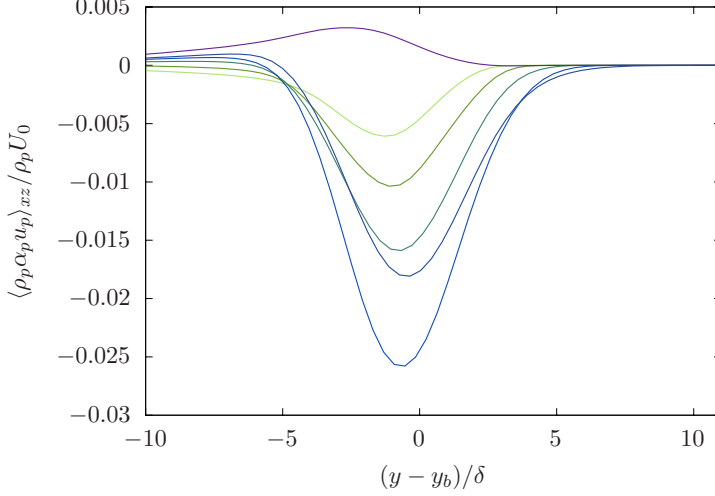


Figure 15: Particle momentum as a function of vertical direction at $Re_\delta = 400$. ($\omega t = 0$, —), ($\omega t = 30$, —), ($\omega t = 60$, —), ($\omega t = 90$, —), ($\omega t = 120$, —), ($\omega t = 150$, —). Significant particle momentum is seen near the bed interface, indicating particle motion at around the bed interface.

0° shows a momentum peak at $1.4d_p$ below the bed interface, and decays to zero by $2.0d_p$ above the bed surface. The momentum peak increases through phases 30, 60, and 90° , and the region of particle transport thickens. Phase 90° shows a momentum peak at $0.46d_p$ below the bed interface, and decays to zero by $5.0d_p$. This indicates a small layer of particles transported close to the bed surface. Phase 120° shows a decreased momentum maximum, and the region of particle transport is thinned. This indicates that particles are slowing and being redeposited in the bed. Phase 150 shows low particle momentum throughout the column, and a reversal in the direction of the momentum. The particles have been redeposited in the bed and are nearly at rest. The mobile particles at certain phases are responsible for the fluid velocity fluctuations observed in 14. Figure 16 shows a top-down view of the particle bed where the particles are colored by their normalized velocities. Beginning at phase 0 degrees, particles are primarily stationary within the bed. By phase 60 degrees the fluid velocity increases and some particles are set into motion, rolling over the bed surface. By phase 90 degrees, a greater number of particles are set in motion, with some rolling over the bed, and some skipping off the bed surface. After this the fluid velocity decreases, as does the particle velocity, until most particles rest in the bed at phase 150 degrees.

At Reynolds 400 the bedform evolves due to particle transport. We use isosurfaces of the fluid-bed interface, $\alpha_{p,b} = 0.2$, shown in figure 17, to visualize the bedform. The bedform is colored by the deviation in local bed height from the average bed height at the corresponding phase. At phase $\omega t = 0^\circ$ to 30° , when the majority of particles are at rest in the bed, we see a relatively flat bed, close to the average bed height throughout the domain. As particles are set into motion small dunes emerge at phase $\omega t = 60^\circ$. These dunes grow in height, to a maximum of one Stokes thickness above or below the average bed height at phase $\omega t = 90^\circ$. After this the particles begin to be redeposited in the bed, and the dunes are reduced. This continues through phase $\omega t = 150^\circ$, which shows only small deviations from the average bed height, and is

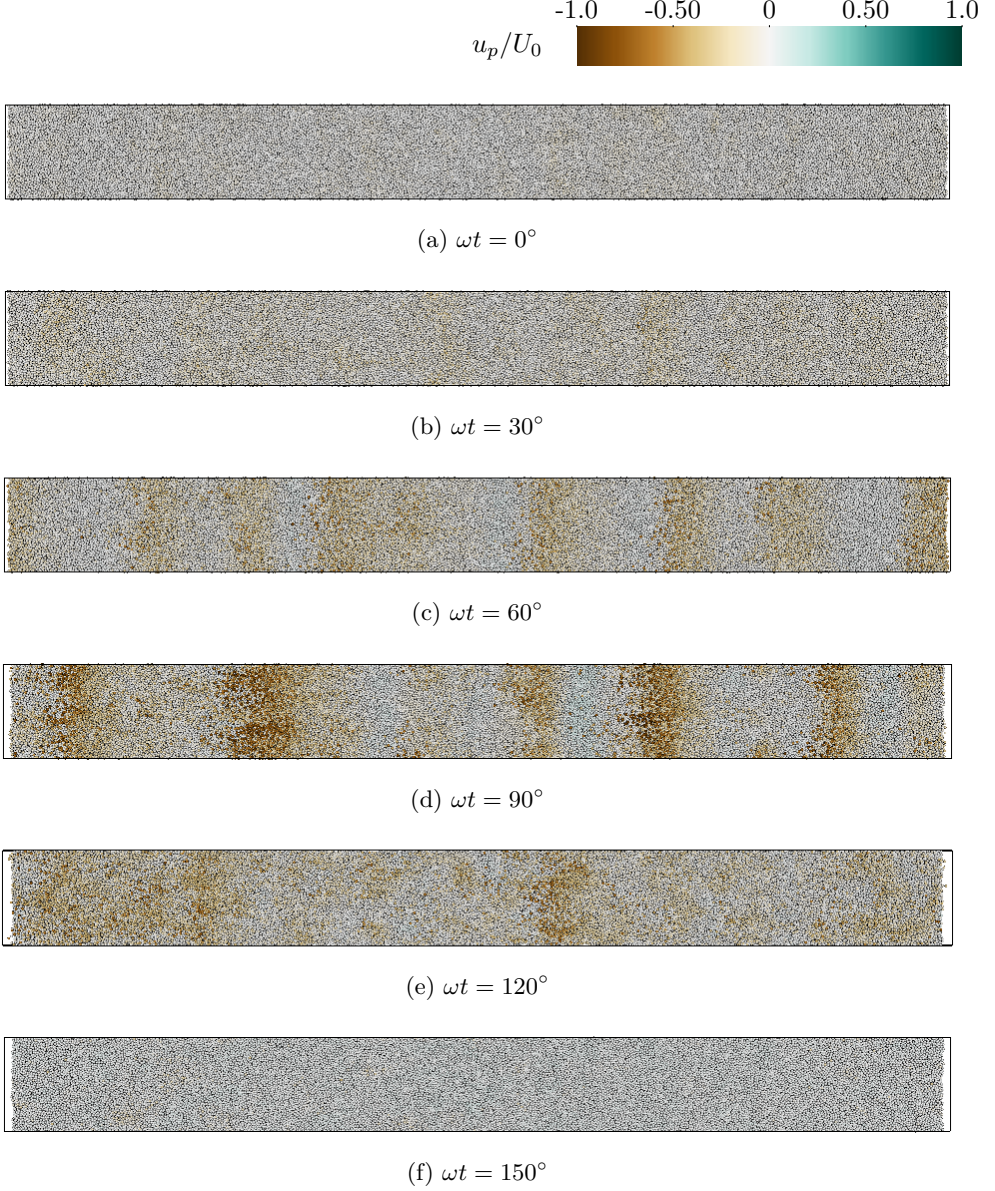


Figure 16: Top-down view of particle bed at $Re_\delta = 400$ and phases 0, 30, 60, 90, 120, 150 degrees. The particles are colored by their normalized stream-wise velocity. Particles are set into motion by the fluid flow, leading to particles rolling over the bed surface.

relatively flat. The presence of hills and dunes at the bed interface may contribute to the increased fluctuations observed at the fluid-bed interface. The coefficient of friction scaled by Re_δ is plotted in figure 18 as a function of time for 400. Compared to the particle free case, Reynolds 400 shows a reduction in coefficient of friction of about 40 percent with a particle bed. The phase shift is 30° . The analytical phase shift for the coefficient of friction in the laminar regime is 45° , showing a departure even at low Reynolds number from the analytical behavior. As with the case at $Re_\delta = 200$,

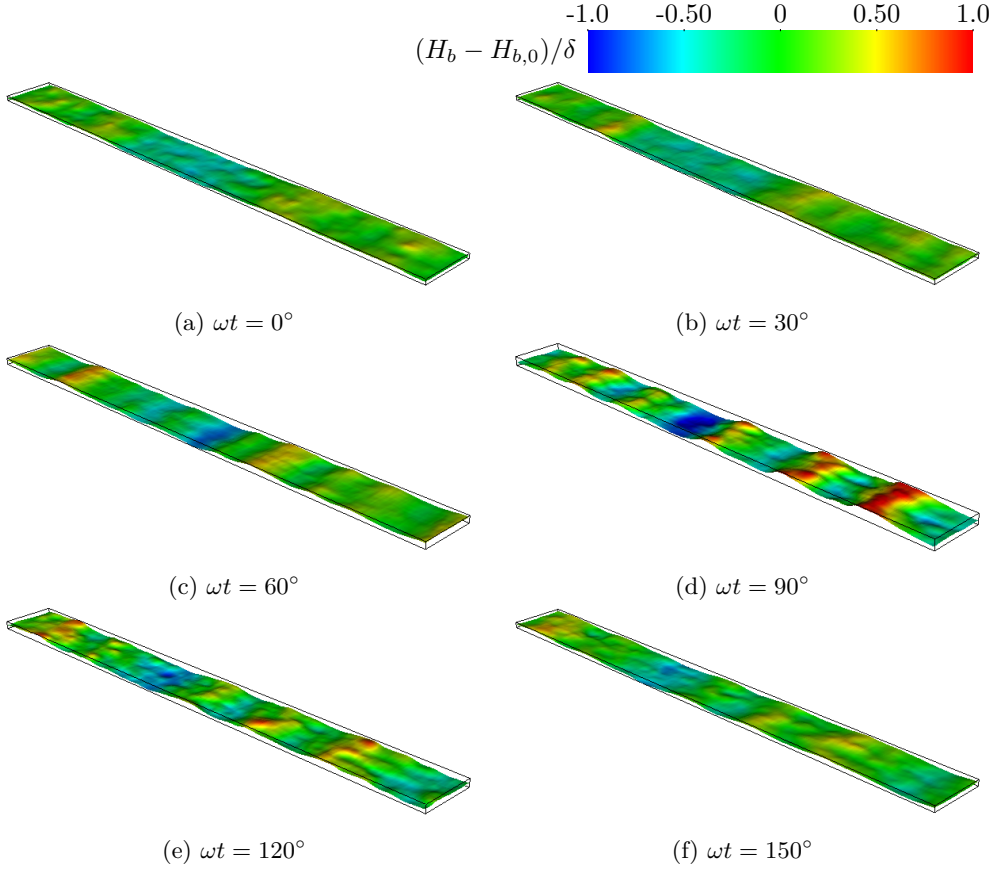


Figure 17: Reynolds 400 bedform height deviations. Small ripples rise and fall below the average bed height.

the reduction in coefficient of friction is caused by the change in boundary condition at the fluid-bed interface.

5.3. Case at $Re_\delta = 800$

At Reynolds 800 the fluid flow is able to set a greater number of particles into motion compared to Reynolds 400. Figure 19 shows a top-down view of the particle bed where the particles are colored by their normalized velocities. The particles first saltate across the bed surface, and then are suspended. Later, as fluctuations decay, the particles are deposited in the bed. The particles are at rest in the bed at phase 0. As the velocity of the flow increases a layer of particles are set in motion, which can be seen at phase 30° . Most of the particles in motion at this point saltate over the top of the bed. As the velocity continues to increase to phase 60° more particles are set in motion. At this phase a large number of the particles are lifted into the flow and transported through the domain. This continues through phase 120° , where the fluid velocity has begun to decrease. As the velocity decreases to phase 150° less particles are in motion, most having been redeposited in the bed. Saltation is once again the dominant mode of particle transport. This cycle continues in the opposite direction in the following half cycle, which is not visualized here. The process of

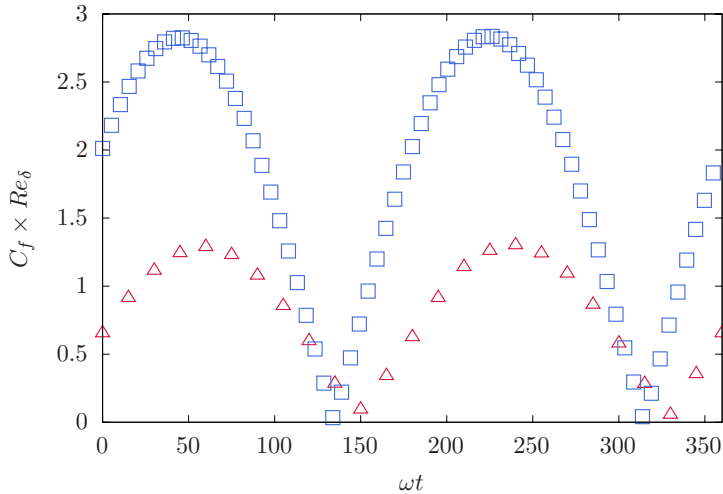


Figure 18: Coefficient of friction for an OBL over a particle bed at $Re_\delta = 400$. Red symbols corresponds to the particle bed case, blue symbols correspond to the smooth wall case. The coefficient of friction is reduced in amplitude nearly half in the presence of a particle bed. The phase is shifted by 30° .

particle transport leads to the formation of ripples in the bed for some phases, while at others, such as phase 90 a transport layer emerges at the top of the bed.

Particle momentum is shown in figure 20 at phases 0, 30, 60, 90, 120, and 150°. For phase $\omega t = 0$ there is small levels of motion from -7.5δ to -2δ deep into the bed. The particle momentum then increases to a maximum at -0.5δ . Afterwards, the particle momentum decreases to zero far from the bed. The particle momentum maximum increases through phases 30, 60 and 90°, and the region of particle transport thickens. The phase $\omega t = 90$ shows negligible particle momentum within the bed up to -3δ from the average bed height. The momentum peaks at -0.5δ for phase 90°, and then decreases to zero near 4δ above the initial bed height. This shows a large number of particles moving with significant velocity at phase 90. The maximum particle momentum decreases for phase 120, and the region of particle transport is thinned. This indicates particle deposition. Phase 150 shows a further decrease in the momentum maximum, to a similar level as in phase 0. The maximum is higher in the flow, however, with small particle transport above the fluid-bed interface. Compared to Reynolds 400, this shows continued particle transport, rather than particles being largely at rest in the bed. Particles are lifted out of the bed and transported in the flow, within a region of six stokes thickness.

Figure 21 shows snapshots of the bed interface. We note that the bed interface forms into dunes that are much larger than those seen at Reynolds 200-400. The dunes expand and roll through the domain. Large numbers of particles are set into motion at certain phases. Those particles are transported through the flow before being deposited into dunes. This is different from the Reynolds 200 case, where the particles only move small amounts and the bedform itself is static. This creates a lower boundary that greatly varies throughout the simulation, and is different from both the smooth wall case and the low Reynolds number cases. That is, the bed interface becomes much more wavy, and at certain phases much of the bed interface

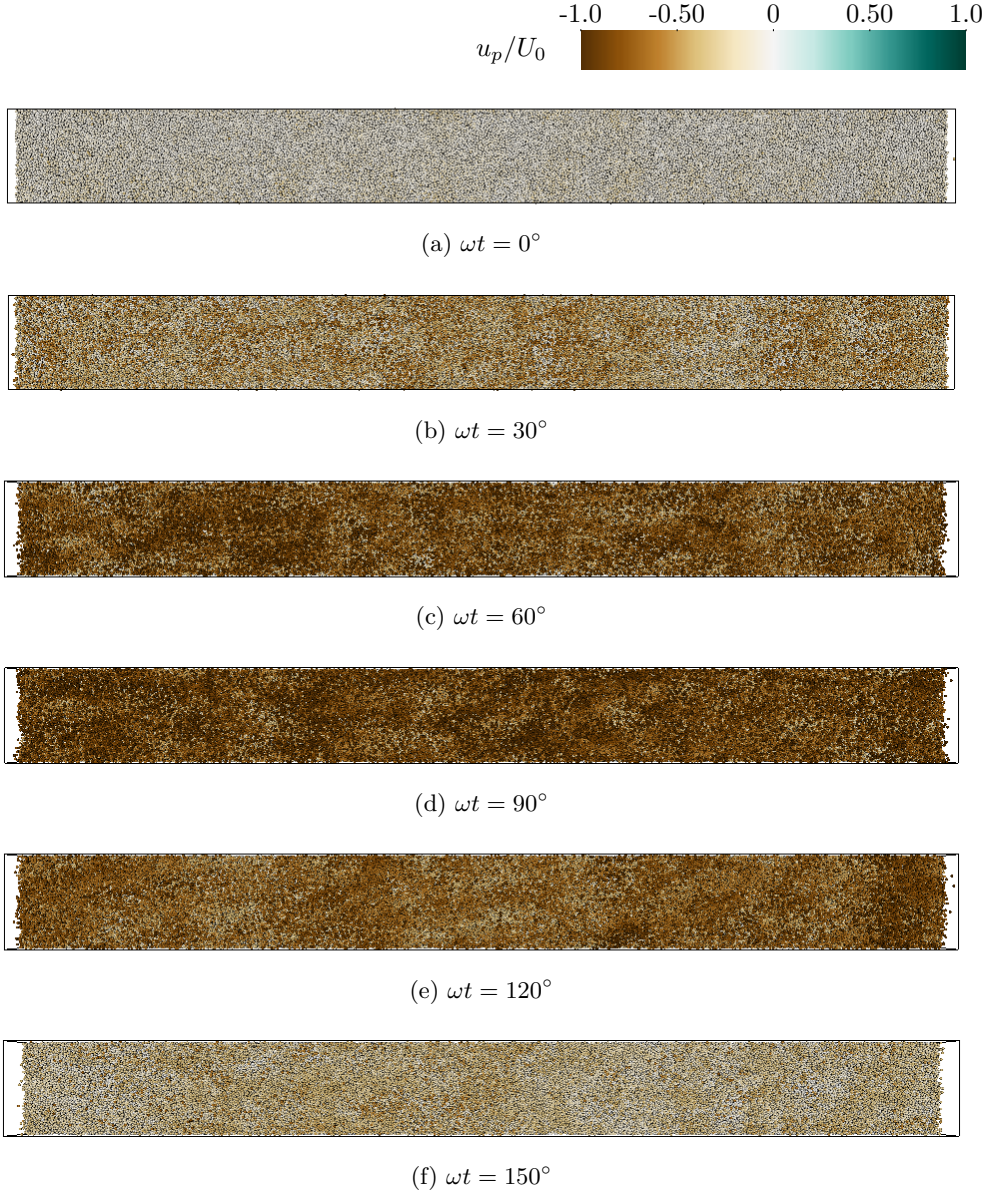


Figure 19: Top-down view of the particle bed at $Re_\delta = 800$ and phases 0, 30, 60, 90, 120, 150 degrees. Particles are colored by their normalized stream-wise velocity. Particles are set into motion and lifted into the flow before being redeposited in the bed, driving bedform evolution.

is sliding across the bed. At other phases there are particles lifted out of the and carried above the interface itself.

At Reynolds 800, the dunes in the bed-form cause greatly increased vortex shedding which leads to stronger turbulence sustained over a larger portion of the period. Figure 22 shows the vorticity at Reynolds 800, overlaid with the isocontour $\alpha_p = \alpha_{p,b}$ denoting the location of the bed-fluid interface. The field drastically deviates from the single phase simulations, with both large scale and small scale structures. The

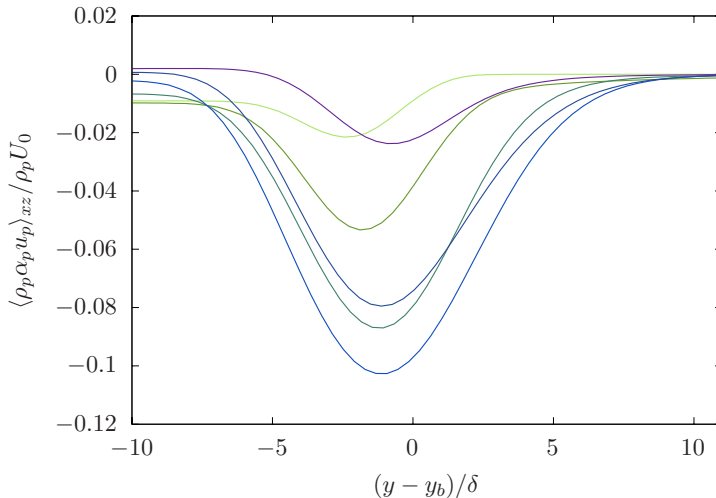


Figure 20: Particle momentum as a function of vertical direction at $Re_\delta = 800$. ($\omega t = 0$, —), ($\omega t = 30$, —), ($\omega t = 60$, —), ($\omega t = 90$, —), ($\omega t = 120$, —), ($\omega t = 150$, —). Particle momentum shows small particle transport near the bed surface for phases 0 and 180° , while phases 90 and 270° show high particle transport in a layer of 6δ .

bed generates vorticity through the small dunes as seen in lower Reynolds numbers. Whereas at low Reynolds numbers the dunes caused large shedding vortices to form in the region just above the bed, Reynolds 800 shows large vortical structures throughout the water column. In the near bed region, at phases 60, 90, and 120° , there are small scale structures. While the smooth wall case also saw significant fluctuations and a range of scales, the fluctuations were not as significant throughout the water column as they are here. The vorticity penetrates deeper into the bed than in the Reynolds 100-400 cases. This indicates greater flow intrusion, large enough at this Reynolds number to cause significant particle transport, as described in Jewel *et al.* (2019). The penetration is most notable at phases 60, 90, and 120° . These correspond to the phases with greatest particle transport, as seen above.

The coefficient of friction is shown in figure 23, scaled by Re_δ . The turbulent eruption can be clearly seen in the single phase case as the dramatic increase in coefficient of friction at phase 75° . In the case of a particle bed there is a clear eruption of turbulence which occurs earlier in the cycle compared to the single phase case, at phase 45° . This represents a phase shift in the turbulent portion of the cycle of 30° . The eruption occurs during the accelerating portion of the cycle, rather than in the decelerating portion as in the smooth wall case. Additionally, where the presence of turbulence leads to an increase in the coefficient of friction compared to the laminar cases in the smooth wall configuration, in the particle bed case the coefficient of friction is decreased in the turbulent case compared to the lower Reynolds number cases. This is due to the flow penetration and transport layer, which reduces the rate the fluid velocity goes to zero within the bed.

The stream-wise velocity is plotted in the figure 24, in semi-logarithmic format. As before, the y direction is re-centered by the average bed height for that phase. In all six cases there is clear flow penetration shown by the nonzero velocity at the bed surface. Indeed, for $\omega t = 60$, 90, and 120° the wall scaled streamwise velocity is 40

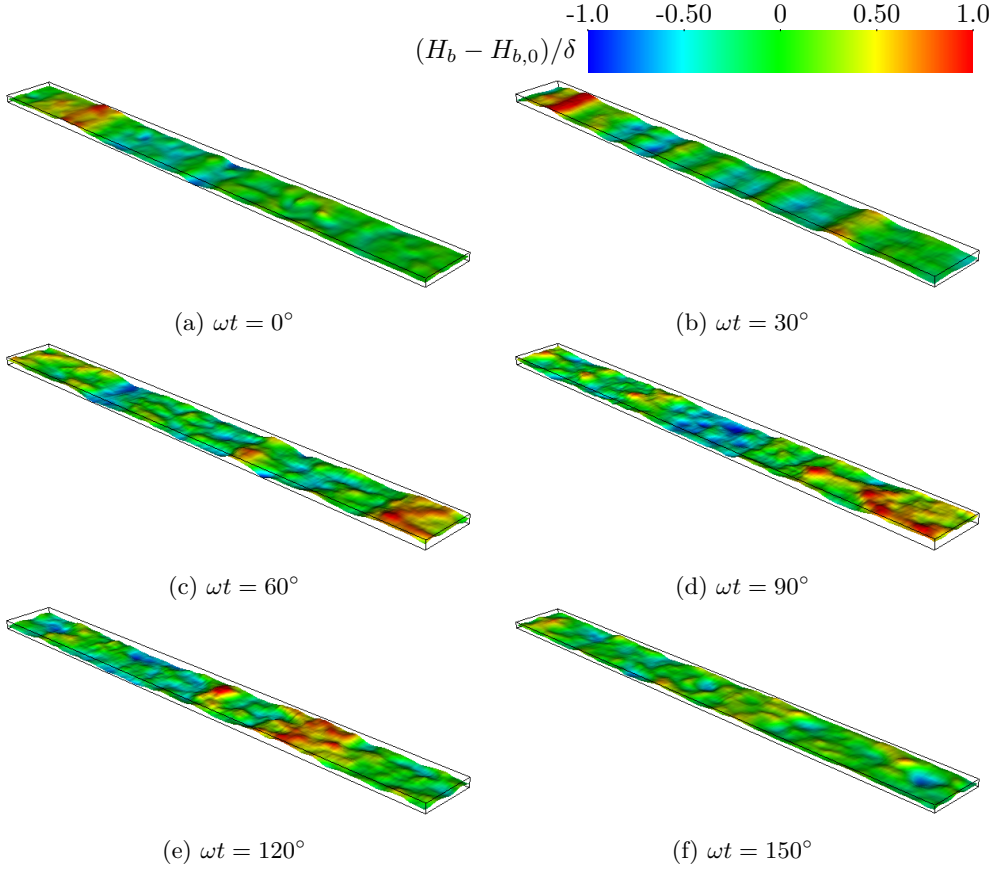


Figure 21: Reynolds 800 bedform height deviations at phases 0, 30, 60, 90, 120, 150. Large dunes rise and fall below the average bed height.

at the bed interface. While we don't observe turbulence at any of the phases shown here, the high flow penetration and

We also show the velocity profiles scaled using the outer scaling, U_0 and δ , seen in 25. This highlights the thickened boundary layer, with a much lower gradient in the bed case than in the smooth wall case. There is an inflection point in the fluid velocity profile. Additionally, we note flow penetration, up to 5δ below the bed interface. The permeability of the particle bed, as well as the particle suspension, represents a very different condition as compared to the no slip and no penetration conditions present for a smooth wall.

As in the low Reynolds cases, the presence of a particle bed leads to greater velocity fluctuations than in the smooth wall cases. Figure 26 shows the stream-wise velocity fluctuations for Reynolds 800. Phase $\omega t = 90^\circ$ shows a thick single peak, at the bed interface. The thickness indicates randomness in the fluctuations, rather than the periodic fluctuations observed at $Re_\delta = 200$. When a particle bed is present, the peak is thicker than in the smooth wall case, which indicates that the random fluctuations are present higher in the water column. At phase $\omega t = 0^\circ$ shows a thick region of fluctuations that extends throughout the water column. This is compared to the smooth wall case, where a similar region of fluctuations extends 12δ away from the wall. While the velocity profiles above show that the flow is no longer turbulent

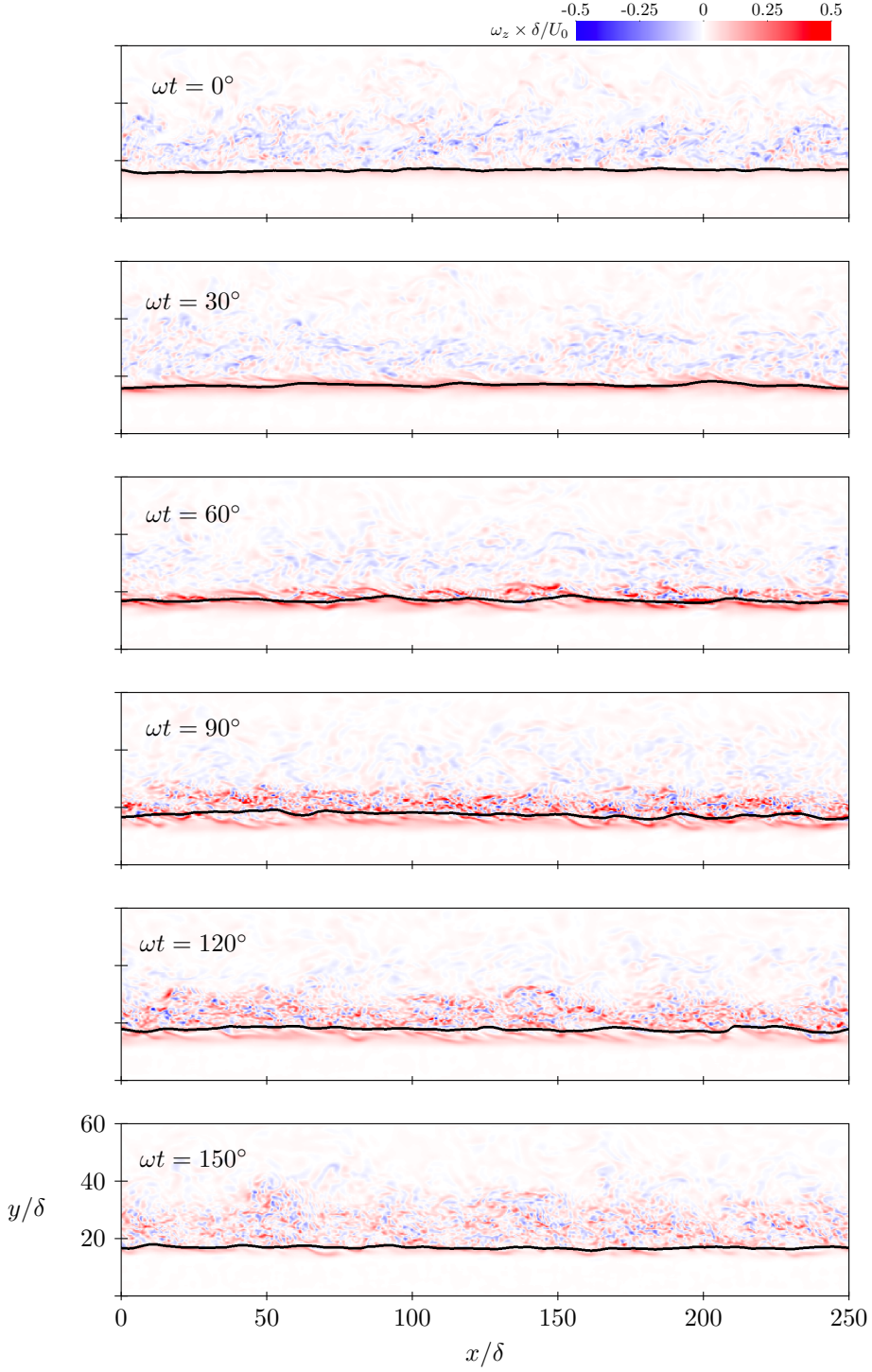


Figure 22: Span-wise vorticity at Re_δ and phases 0, 30, 60, 90, 120, and 150 degrees. The bedform shifts into dunes at various phases. The shedding vortices create a large range of scales. The eddies penetrate the bed interface.

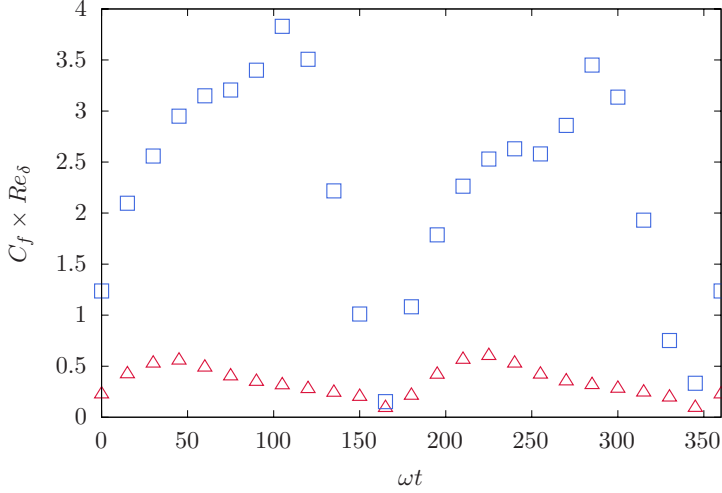


Figure 23: Coefficient of friction for an OBL over a particle bed at $Re_\delta = 800$. Red symbols represent particle-laden flow, blue symbols represent single phase flow. The particle bed significantly reduces coefficient of friction.

at these phase $\omega t = 0^\circ$ fluctuations remain throughout the water column. The high fluctuations and thicker region of fluctuations indicate a greater level of turbulence in the presence of a particle bed as compared to the smooth wall case.

6. Conclusions

We investigate the mechanisms by which a particle bed modifies the oscillatory boundary layer. Using Euler-Lagrange simulations of an OBL over a particle bed at Reynolds numbers $Re_\delta = 200, 400$, and 800 , density ratio $\rho_p/\rho_f = 2.65$, maximum Shields numbers ranging from 1.42×10^{-2} to 7.40×10^{-2} , Galileo number $Ga = 51.9$, Stokes number ranging from 3.99 to 15.97 , and Kuelegan-Carpenter number ranging from 1.7×10^3 to 6.8×10^3 , and showed large modulation to the underlying boundary layer. Additionally, we performed simulations with a smooth wall to provide a benchmark of the OBL for comparison with the OBL over a particle bed. We observed two mechanisms of modulation to the boundary layer: (I) the permeability of the bedform allows fluid flow to penetrate into the bed, causing an expansion of the boundary layer, and (II) resuspension of particles at high Reynolds number leads to significant fluctuations in the fluid phase, as a result of the feedback force exerted by the particle.

For the case at $Re_\delta = 200$, there is significant flow modulation, despite a stationary bed. In comparison to the case of an OBL over a smooth, impermeable wall, we observe significant velocity fluctuations, changes to the velocity profile, and reduction in coefficient of friction. These changes are due to the permeability of the bed and the rough wavy fluid-bed interface. The bed permeability allows flow penetration, which creates a slip velocity at the bed-fluid interface, an inflection point in the velocity profile, and an expansion of the boundary layer. The alteration of the velocity profile drives a reduction in the coefficient of friction by nearly half. This, in turn leads to reduced Shields numbers compared to predictions from cases with an impermeable wall, be it smooth, rough, or wavy.

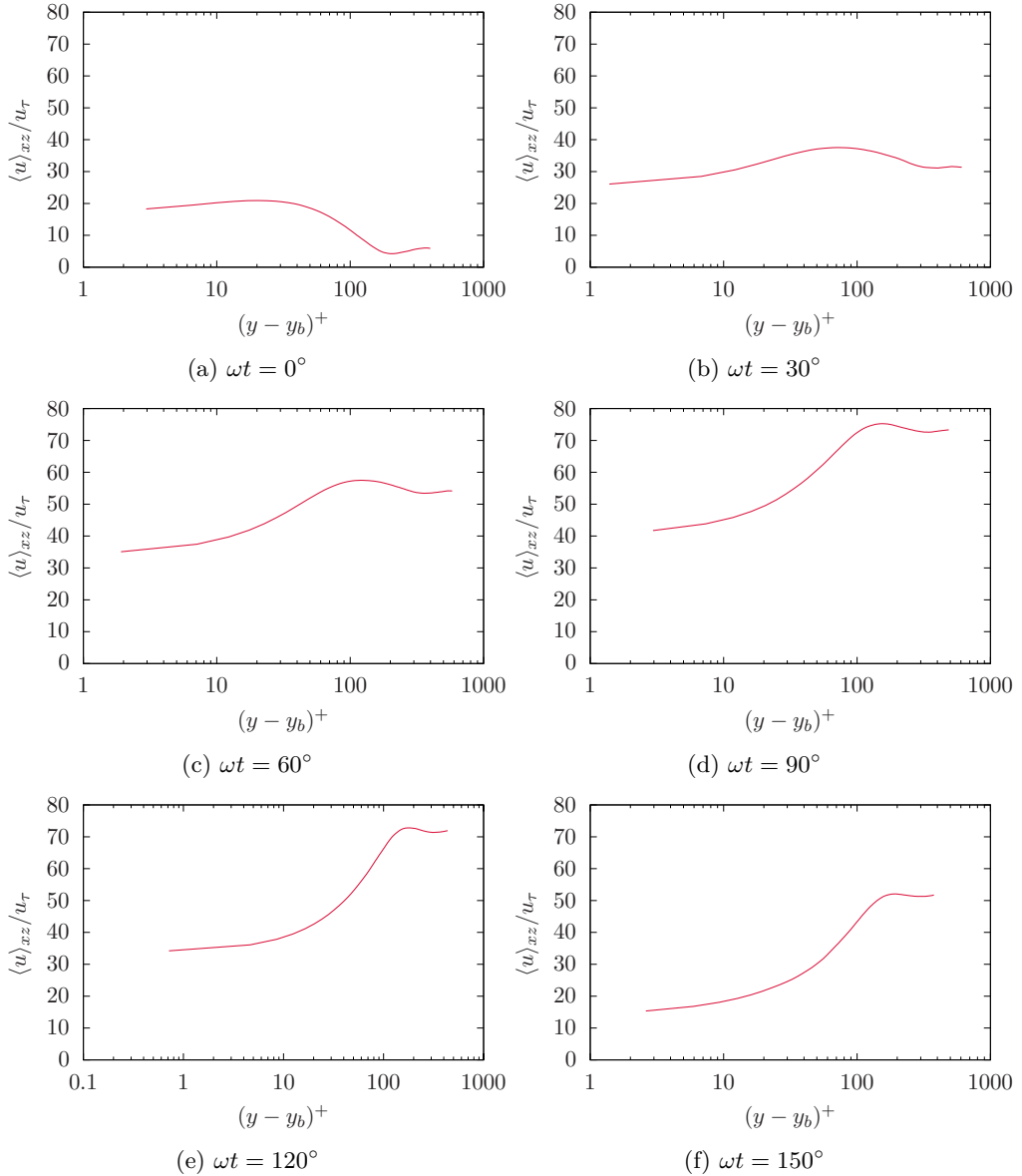


Figure 24: Streamwise velocity profile for Reynolds 800. There is no logarithmic layer present.

The case at $Re_\delta = 400$ has a greater extent of flow penetration, and a thicker boundary layer. The coefficient of friction is reduced by nearly half. In this case, the particle transport is cyclic. The particles are at rest when the fluid velocity is minimum. As the latter increases, the particles are set into motion and the saltate over the particle bed. This leads to an evolving bedform and the emergence of dunes. These dunes contribute to vortex shedding, in contrast to the smooth wall case, where no vortex shedding is observed. The particle transport also contributes to the increased fluid velocity fluctuations through the particle feedback force, as evidenced by the correspondence of particle momentum and fluid velocity fluctuation peaks.

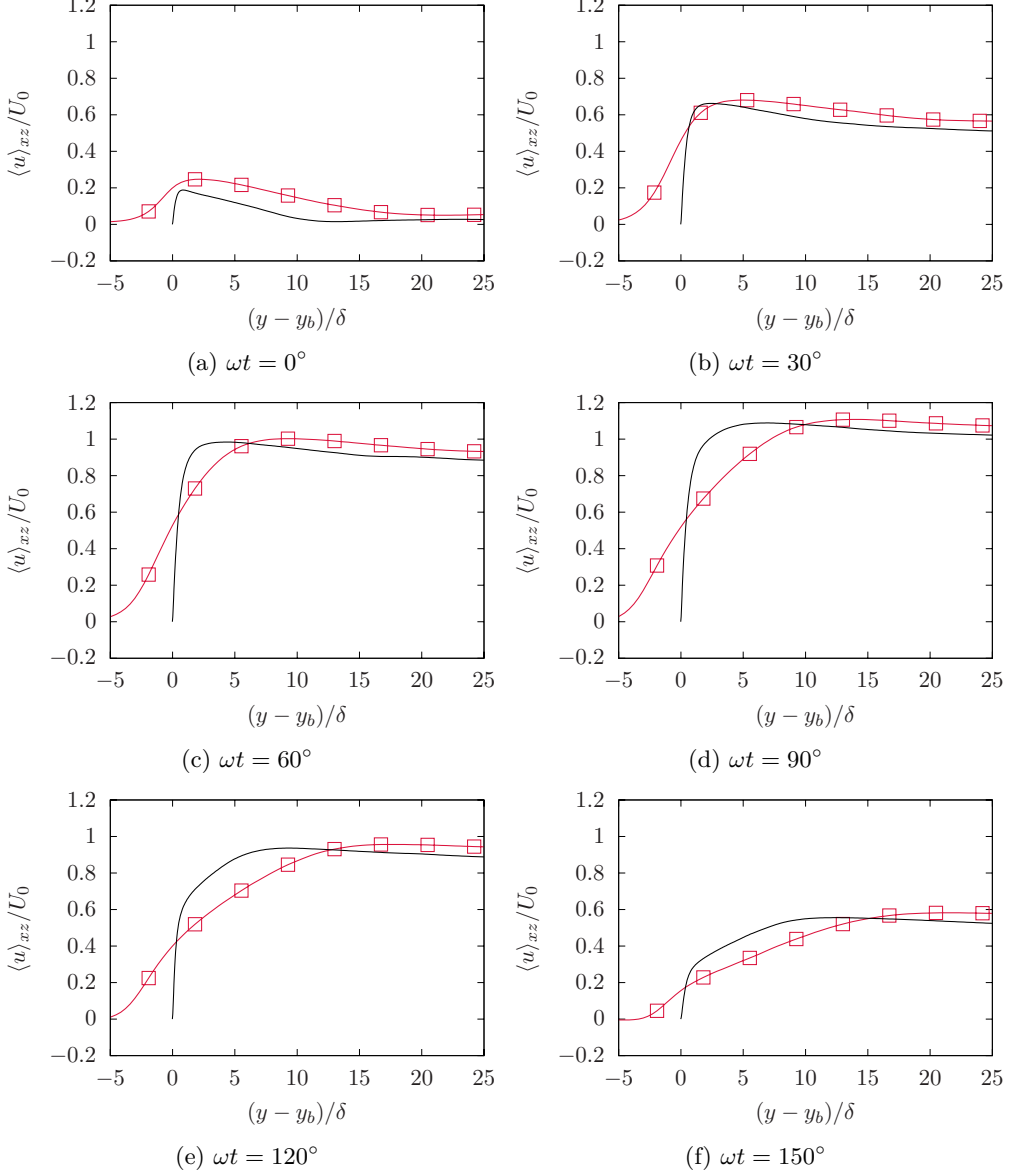


Figure 25: Profiles of the mean streamwise velocity at $Re_\delta = 800$. The profiles are given at phases 0, 30, 60, 90, 120, and 150. Red lines with symbols correspond to simulations with a particle bed, black lines correspond to smooth wall simulations.

For $Re_\delta = 800$, we see more particles set in motion over a greater portion of the period and higher above the bed surface. The maximum particle momentum is near 3 times as at $Re_\delta = 400$. Particle transport is still cyclic. The particles are at rest when the fluid velocity is minimum. As the fluid velocity increases, particles are set into motion and saltate over the bed, as at $Re_\delta = 400$. This leads to dune formation as before, but then gives way to particle resuspension. The particles are transported in a layer of the flow above the particle bed. As the fluid velocity decreases, particles

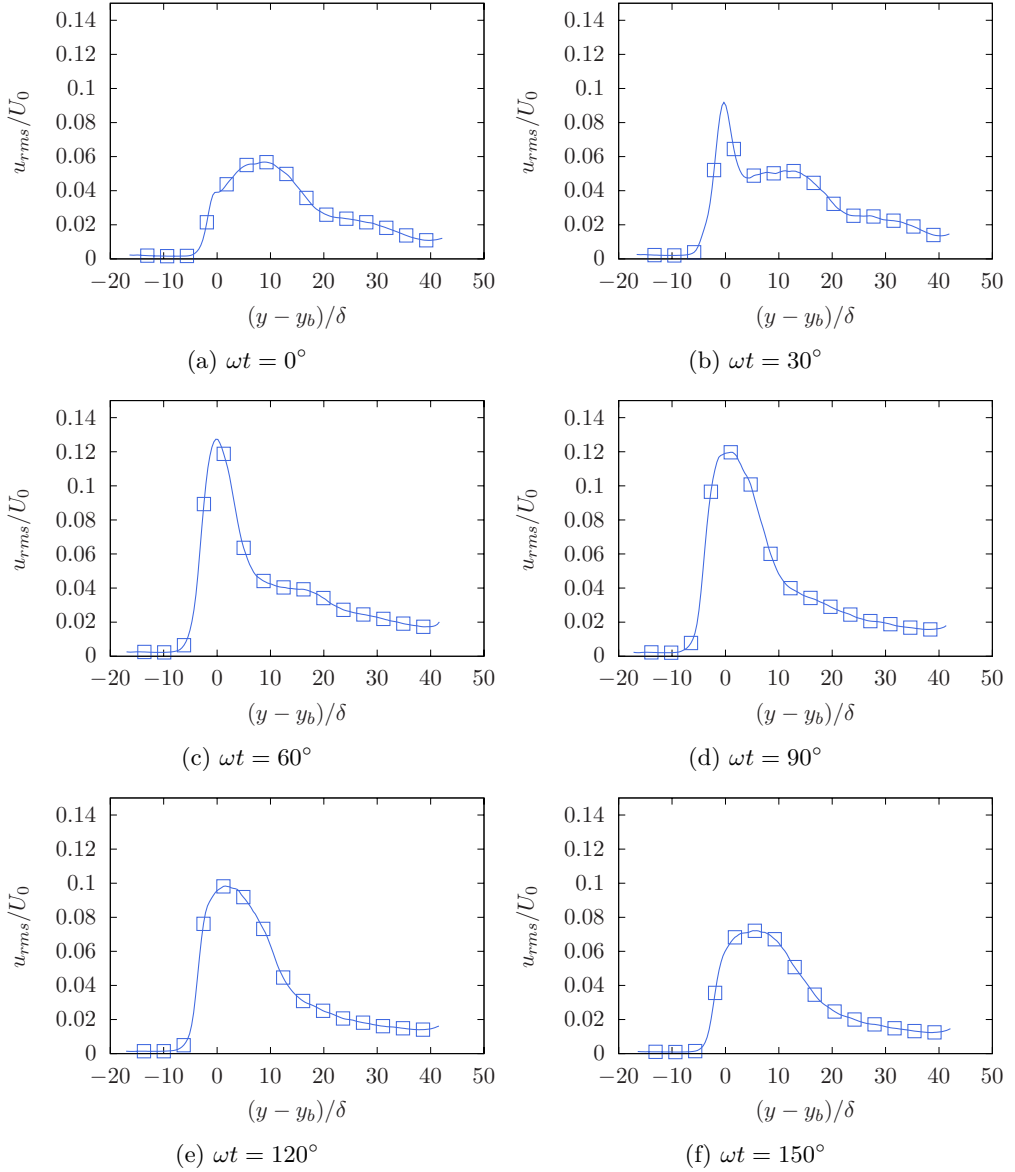


Figure 26: Profiles of the rms fluctuations of the streamwise velocity at $Re_\delta = 800$. The profiles are given at phases 0, 30, 60, 90, 120, and 150. Velocity fluctuations show a thick single peak near the bed, indicating randomness in the fluctuations.

slow and are redeposited in the bed. This creates a boundary layer that is much thicker than the smooth wall case, an inflection point in the velocity profile and a lower slope in the velocity profile in the boundary layer. The alteration to the fluid velocity profile causes a drastic reduction in the coefficient of friction, by nearly an eighth. Instead of the increased fluctuations accompanying an increase in the coefficient of friction, as in the smooth, impermeable wall case, the particle bed case shows a reduction in the coefficient of friction. This is an important departure from

the known OBL behavior over an impermeable wall for the intermittent turbulent regime. The maximum fluctuations are associated with maximum particle transport. The region of particle transport is associated with the region of velocity fluctuations, showing that the particle feedback force contributes to the increased fluctuations.

These results show that the permeability of the particle bed introduces additional physics which are not well captured by impermeable wall treatments, even if the wall has some degree of roughness and waviness. Predictions of sediment transport may be inaccurate if the bed permeability is ignored, as inclusion of permeability leads to lower coefficient of friction, and thereby the Shields number.

Acknowledgements. Computing resources through ACCESS award EES230041 and Research Computing at Arizona State University are gratefully acknowledged.

Funding. This research received no specific grant from any funding agency, commercial or not-for-profit sectors.

Declaration of interests. The authors report no conflict of interest.

Author ORCIDs. M. H. Kasbaoui, <https://orcid.org/0000-0002-3102-0624>;

REFERENCES

- AKHAVAN, R., KAMM, R. D. & SHAPIRO, A. H. 1991*a* An investigation of transition to turbulence in bounded oscillatory Stokes flows Part 1. Experiments. *Journal of Fluid Mechanics* **225**, 395–422.
- AKHAVAN, R., KAMM, R. D. & SHAPIRO, A. H. 1991*b* An investigation of transition to turbulence in bounded oscillatory Stokes flows Part 2. Numerical simulations. *Journal of Fluid Mechanics* **225**, 423–444.
- ANDERSON, T. B. & JACKSON, R. 1967 Fluid Mechanical Description of Fluidized Beds. Equations of Motion. *Industrial & Engineering Chemistry Fundamentals* **6** (4), 527–539.
- AROLLA, S. K. & DESJARDINS, O. 2015 Transport modeling of sedimenting particles in a turbulent pipe flow using Euler–Lagrange large eddy simulation. *International Journal of Multiphase Flow* **75**, 1–11.
- BLENNERHASSETT, P. J. & BASSOM, A. P. 2002 The linear stability of flat Stokes layers. *Journal of Fluid Mechanics* **464**, 393–410.
- BLONDEAUX, P. & SEMINARA, G. 1979 Transizione incipiente al fondo di un’onda di gravità. *Atti della Accademia Nazionale dei Lincei. Classe di Scienze Fisiche, Matematiche e Naturali. Rendiconti* **67** (6), 408–417.
- CAPECELATRO, J. & DESJARDINS, O. 2013 An Euler–Lagrange strategy for simulating particle-laden flows. *Journal of Computational Physics* **238**, 1–31.
- CARSTENSEN, S., SUMER, B. M. & FREDSE, J. 2010 Coherent structures in wave boundary layers. Part 1. Oscillatory motion. *Journal of Fluid Mechanics* **646**, 169–206.
- CARSTENSEN, S., SUMER, B. M. & FREDSE, J. 2012 A note on turbulent spots over a rough bed in wave boundary layers. *Physics of Fluids* **24** (11), 115104.
- CHIODI, FILIPPO, CLAUDIN, PHILIPPE & ANDREOTTI, BRUNO 2014 A two-phase flow model of sediment transport: Transition from bedload to suspended load. *Journal of Fluid Mechanics* **755**, 561–581, arXiv: 1401.0807.
- COSTAMAGNA, P., VITTORI, G. & BLONDEAUX, P. 2003 Coherent structures in oscillatory boundary layers. *Journal of Fluid Mechanics* **474**, 1–33.
- FINN, J. R. & LI, M. 2016 Regimes of sediment-turbulence interaction and guidelines for simulating the multiphase bottom boundary layer. *International Journal of Multiphase Flow* **85**, 278–283.
- FINN, J. R., LI, M. & APTE, S. V. 2016 Particle based modelling and simulation of natural sand dynamics in the wave bottom boundary layer. *Journal of Fluid Mechanics* **796**, 340–385.
- FYTANIDIS, D. K., GARCÍA, M. H. & FISCHER, P. F. 2021 Mean flow structure and velocity–bed shear stress maxima phase difference in smooth wall, transitionally turbulent oscillatory boundary layers: Direct numerical simulations. *Journal of Fluid Mechanics* **928**, A33.

- GHODKE, C. D. & APTE, S. V. 2016 DNS study of particle-bed-turbulence interactions in an oscillatory wall-bounded flow. *Journal of Fluid Mechanics* **792**, 232–251.
- GHODKE, C. D. & APTE, S. V. 2018 Roughness effects on the second-order turbulence statistics in oscillatory flows. *Computers & Fluids* **162**, 160–170.
- GIBILARO, L. G., GALLUCCI, K., DI FELICE, R. & PAGLIAI, P. 2007 On the apparent viscosity of a fluidized bed. *Chemical Engineering Science* **62** (1), 294–300.
- HINO, M., SAWAMOTO, M. & TAKASU, S. 1976 Experiments on transition to turbulence in an oscillatory pipe flow. *Journal of Fluid Mechanics* **75** (2), 193–207.
- JENSEN, B. L., SUMER, B. M. & FREDSE, J. 1989 Turbulent oscillatory boundary layers at high Reynolds numbers. *Journal of Fluid Mechanics* **206**, 265–297.
- JEWEL, A., FUJISAWA, K. & MURAKAMI, A. 2019 Effect of seepage flow on incipient motion of sand particles in a bed subjected to surface flow. *Journal of Hydrology* **579**, 124178.
- KASBAOUI, M., HOUSSEM, KOCH, DONALD L. & DESJARDINS, OLIVIER 2019 Clustering in Euler–Euler and Euler–Lagrange simulations of unbounded homogeneous particle-laden shear. *Journal of Fluid Mechanics* **859**, 174–203.
- KIDANEMARIAM, A. G. & UHLMANN, M. 2014 Interface-resolved direct numerical simulation of the erosion of a sediment bed sheared by laminar channel flow. *International Journal of Multiphase Flow* **67**, 174–188.
- LEE, CHENG-HSIEN, LOW, YING MIN & CHIEW, YEE-MENG 2016 Multi-dimensional rheology-based two-phase model for sediment transport and applications to sheet flow and pipeline scour. *Physics of Fluids* **28** (5), 053305.
- MAURIN, RAPHAEL, CHAUCHAT, JULIEN & FREY, PHILIPPE 2016 Dense granular flow rheology in turbulent bedload transport. *Journal of Fluid Mechanics* **804**, 490–512, arXiv: 1602.06712.
- MAXEY, MARTIN R. & RILEY, JAMES J. 1983 Equation of motion for a small rigid sphere in a nonuniform flow. *The Physics of Fluids* **26** (4), 883–889.
- MAZZUOLI, M., BLONDEAUX, P., VITTORI, G., UHLMANN, M., SIMEONOV, J. & CALANTONI, J. 2020 Interface-resolved direct numerical simulations of sediment transport in a turbulent oscillatory boundary layer. *Journal of Fluid Mechanics* **885**.
- MAZZUOLI, M., KIDANEMARIAM, A. G., BLONDEAUX, P., VITTORI, G. & UHLMANN, M. 2016 On the formation of sediment chains in an oscillatory boundary layer. *Journal of Fluid Mechanics* **789**, 461–480.
- MAZZUOLI, M. & VITTORI, G. 2019 Turbulent spots in an oscillatory flow over a rough wall. *European Journal of Mechanics - B/Fluids* **78**, 161–168.
- OZDEMIR, C., HSU, T. J. & BALACHANDAR, S. 2014 Direct numerical simulations of transition and turbulence in smooth-walled Stokes boundary layer. *Physics of Fluids* **26**.
- PEDOCCHI, F., CANTERO, M. I. & GARCÍA, M. H. 2011 Turbulent kinetic energy balance of an oscillatory boundary layer in the transition to the fully turbulent regime. *Journal of Turbulence* **12**, N32.
- SALON, S., ARMENIO, V. & CRISE, A. 2007 A numerical investigation of the Stokes boundary layer in the turbulent regime. *Journal of Fluid Mechanics* **570**, 253–296.
- SARPKAYA, T. 1993 Coherent structures in oscillatory boundary layers. *Journal of Fluid Mechanics* **253**, 105–140.
- SCOTT, G. D. & KILGOUR, D. M. 1969 The density of random close packing of spheres. *Journal of Physics D: Applied Physics* **2** (6), 863–866.
- STOKES, G. G. 1855 On the effects of internal friction of fluids on the motion of pendulums. *Transactions of the Cambridge Philosophical Society* **9**.
- TENNETI, S., GARG, R. & SUBRAMANIAM, S. 2011 Drag law for monodisperse gas–solid systems using particle-resolved direct numerical simulation of flow past fixed assemblies of spheres. *International Journal of Multiphase Flow* **37** (9), 1072–1092.
- VITTORI, G., BLONDEAUX, P., MAZZUOLI, M., SIMEONOV, J. & CALANTONI, J. 2020 Sediment transport under oscillatory flows. *International Journal of Multiphase Flow* **133**, 103454.
- VITTORI, G. & VERZICCO, R. 1998 Direct simulation of transition in an oscillatory boundary layer. *Journal of Fluid Mechanics* **371**, 207–232.
- XIONG, CHENGWANG, QI, XIANG, GAO, ANKANG, XU, HUI, REN, CHENGJIAO & CHENG, LIANG 2020 The bypass transition mechanism of the Stokes boundary layer in the intermittently turbulent regime. *Journal of Fluid Mechanics* **896**, A4.